Recent Progress in Two-Dimensional Materials for Electrocatalytic CO$_2$ Reduction

Song Lu [1], Fengliu Lou [2] and Zhixin Yu [1,*]

[1] Department of Energy and Petroleum Engineering, University of Stavanger, 4036 Stavanger, Norway; song.lu@uis.no

[2] Beyonder AS, Kanalsletta 2, 4033 Stavanger, Norway; fengliu@beyonder.no

[*] Correspondence: zhixin.yu@uis.no; Tel.: +47-51832238

Abstract: Electrocatalytic CO$_2$ reduction (ECR) is an attractive approach to convert atmospheric CO$_2$ to value-added chemicals and fuels. However, this process is still hindered by sluggish CO$_2$ reaction kinetics and the lack of efficient electrocatalysts. Therefore, new strategies for electrocatalyst design should be developed to solve these problems. Two-dimensional (2D) materials possess great potential in ECR because of their unique electronic and structural properties, excellent electrical conductivity, high atomic utilization and high specific surface area. In this review, we summarize the recent progress on 2D electrocatalysts applied in ECR. We first give a brief description of ECR fundamentals and then discuss in detail the development of different types of 2D electrocatalysts for ECR, including metal, graphene-based materials, transition metal dichalcogenides (TMDs), metal–organic frameworks (MOFs), metal oxide nanosheets and 2D materials incorporated with single atoms as single-atom catalysts (SACs). Metals, such as Ag, Cu, Au, Pt and Pd, graphene-based materials, metal-doped nitric carbide, TMDs and MOFs can mostly only produce CO with a Faradic efficiencies (FE) of 80~90%. Particularly, SACs can exhibit FEs of CO higher than 90%. Metal oxides and graphene-based materials can produce HCOOH, but the FEs are generally lower than that of CO. Only Cu-based materials can produce high carbon products such as C$_2$H$_4$ but they have low product selectivity. It was proposed that the design and synthesis of novel 2D materials for ECR should be based on thorough understanding of the reaction mechanism through combined theoretical prediction with experimental study, especially in situ characterization techniques. The gap between laboratory synthesis and large-scale production of 2D materials also needs to be closed for commercial applications.

Keywords: carbon dioxide; two-dimensional materials; electrocatalytic reduction; graphene; TMD; MOF; metal oxide nanosheet; SAC

1. Introduction

CO$_2$ is the main component of greenhouse gases which lead to environmental concerns, and its concentration has increased from approximately 280 ppm in the early 1800s to 410 ppm today [1–3]. Without proper strategies to combat this problem, the steadily growing CO$_2$ emissions will arouse the increase in the global average temperature, loss of glaciers, rise of sea level and other climate issues [4]. To reverse these negative courses, technologies such as carbon capture and storage (CCS) have been pursued [5–7]. Despite tremendous efforts on CCS, including separating CO$_2$ from air or flue gas, storing the captured CO$_2$ is still a daunting challenge due to the risk of leakage, massive energy consumption, high cost and social acceptance [8–12]. An alternative approach is to utilize CO$_2$ as raw material and convert it into value-added products, which approach has received extensive attention in the past decades [13–15]. Therefore, the conversion of CO$_2$ has been regarded as a promising route for closing the carbon cycle and producing value-added chemicals and fuels.

The conversion of CO_2 can be realized by a variety of technologies such as thermo-chemical, electrochemical, photochemical, radiochemical and biochemical reactions [16–24]. Among these, the reduction of CO_2 by electrochemical strategies is attractive and exhibits many advantages [25,26]. For instance, the energy required for electrochemical reduction reactions can be provided by renewable energy such as solar, geothermal or wind energy. In addition, the reaction can be performed under ambient pressure and temperature. Moreover, the external voltages as well as electrolyte solutions can be adjusted to produce specific products. However, the physicochemical properties of the CO_2 molecule make electrochemical conversion processes challenging. To convert CO_2 into other products, the dissociation of the C=O bond is essential and must overcome high-energy barriers of about 750 kJ/mol. In addition, electrolyte solutions are generally water-based, which makes the reaction inefficient due to the poor CO_2 dissolution in water. In the past decades, both theoretical and experimental work have disclosed that the electrocatalysts play a vital role in catalytic processes [27–32]. For example, it has been proven that traditional metal electrocatalysts, such as copper, platinum and gold, can activate CO_2 and reduce it into valuable chemical products [33–35]. However, these catalysts suffer drawbacks such as high overpotential, poor stability, low selectivity, complex separation and low efficiency for specific products. In addition, the prices of precious metals hamper the large-scale application of Pt catalysts. Therefore, developing efficient, cost-effective and durable alternatives to the traditional metal catalysts for electrocatalytic CO_2 reduction (ECR) reaction is urgent.

In recent years, two-dimensional (2D) materials with novel geometric, electronic and optical properties greatly accelerated the development of catalysts. Two-dimensional materials, sometimes referred to as single-layer materials, are crystalline materials consisting of a single layer of atoms. These materials have promising applications in fields such as photovoltaics, semiconductors, electrodes and water purification. Two-dimensional materials can be categorized as either 2D allotropes of various elements or as compounds consisting of two or more covalently bonded elements. The elemental 2D materials generally carry the -ene suffix in their names, while the compounds have -ane or -ide suffixes. A wide range of 2D compounds, including metals, chalcogenides, group IV and V elements, oxides, carbides, nitrides, halides, hydroxides, hydrides, phosphates, phosphonates and covalent organic frameworks, have been investigated for various applications. Two-dimensional materials can exhibit semiconductive, insulative or even metallic behavior. Some of them with direct or indirect band gaps have great responses to ultraviolet and visible light. The electronic and optical properties of these 2D materials are tunable by adjusting the number of layers because of quantum confinement. Two-dimensional semiconductive materials display strong enhancements of Coulomb interactions among charge carriers and defects, contributing to longer-lived excitons compared to their bulk structures [36]. The specific surface area of 2D materials is usually quite high and more active atoms can be exposed. The physicochemical properties of 2D materials, especially, can be effectively modulated by different engineering strategies, including heterostructure, doping, chemical functionalization, etc. [37].

When employed as catalysts, 2D materials with nanosheets can show unique properties and excellent performance in catalytic reactions. Compared with conventional bulk materials, they have much higher specific surface areas and high percentages of bare surface atoms that can offer abundant active sites, boosting catalytic reactions. Note that the highly exposed surface atoms can potentially escape and form defect structures, leading to decreased coordination numbers of surface atoms, which are the preferential sites for the adsorption of reactants or intermediates. Similarly, the edge atoms of nanosheets with low coordination numbers can also exhibit novel catalytic properties. Therefore, 2D structures can promote the chemisorption of reactants and improve catalytic performance. A large class of 2D materials, such as noble metals, metal oxides, graphene, graphite carbon nitride (g–C_3N_4), transition metal dichalcogenides (TMDs), metal–organic frameworks (MOFs), etc., has been demonstrated to have great potential to catalyze CO_2 conversion

reactions [38–43]. Particularly, graphene, known as the first invented 2D material, has attracted extensive attention for many applications [44]. Its unique mechanical characteristics, electronic structures and optical properties make it applicable in fields such as solar cells, LED transistors, sensors and catalysts [45–48]. More importantly, the properties of 2D materials can be easily tuned via doping atoms, hybridizing with other nanostructures, surface engineering and defect generation, further improving their electronic properties and catalytic performance.

Numerous studies have been reported for ECR, and a few excellent reviews have been published. For example, Wang et al. reviewed the principles for electrocatalyst design and performance evaluation as well as the factors influencing ECR activity [49]. Nitopi et al. described the various experimental and theoretical approaches used to explore the mechanisms for the formation of ECR products on Cu catalysts. They concluded that nanostructuring and constructing bimetallic electrodes can be effective strategies to enhance activity and selectivity of Cu based catalysts [50]. Jin et al. highlighted the utilization of in situ spectroscopy, including X-ray absorption, X-ray photoelectron, Raman, infrared and mass spectroscopy, which greatly refined the understanding of ECR from intermediates, reaction pathways, active sites and the effects of a reaction environment on product distribution [51]. Zhu et al. summarized controlled synthesis methods for embedding a single atom on different carbon materials as an ECR catalyst. The effects of precursors and preparation environments on the structure of single-atom catalysts (SACs) were discussed. They also compared the intrinsic activity of different metal centers and methods for enhancing ECR efficiency [52]. Zhu et al. reviewed the latest progress on developing 2D materials for ECR from the perspective of theoretical simulation and discussed the reaction mechanisms of various 2D materials for ECR [53]. Zhang et al. reviewed recent advances on materials development for CO_2 conversion by thermocatalysis, photocatalysis and photothermocatalysis, highlighting the reaction pathways and mechanism on C=O bond activation and intermediate formation [54]. Very recently, they also summarized CO_2 conversion by electro- and photoelectrocatalysis, emphasizing the importance of operando characterization theoretical simulations [55]. Li et al. briefly reviewed bimetallic chalcogenides for ECR application in the past five years [56]. They disclosed that hybridization between metal atoms, such as that of intermetallic compounds, heterostructures and metal doping, shows positive effects on ECR selectivity and activity. Wang et al. reviewed recent advances on non-noble-metal-based ECR catalysts, focusing on the synthesis strategies for engineering the electrocatalysts and the ECR mechanism [57]. Therefore, a wide range of topics have been covered for ECR. In this work, we systematically review the recent progress on both theoretical and experimental work on 2D materials applied in ECR according to the materials type. We start with the introduction to 2D materials and CO_2 conversion as well as the fundamentals of ECR. Thereafter, the emerging 2D materials for ECR, including metal, graphene-based materials, TMDs, MOFs, metal oxides and single-atom anchored 2D materials, are discussed in detail, and the effects of structure and modification strategies on catalytic performance for ECR are emphasized. We also summarize GDE and MEA electrolyzers which could solve the problem of limited CO_2 solubility and energy loss of conventional H-type cells for potential industrial ECR applications. Based on these, future perspectives for ECR catalysts design and synthesis are proposed. We aim for this contribution to enlighten future research directions and strategies for exploiting novel 2D materials for ECR and energy conversion in general.

2. Fundamentals of Electrochemical CO_2 Reduction

2.1. CO_2 Properties and the Reduction Products

CO_2 is one of the most stable molecules with a strong O=C=O double bond, and its bond energy is higher than that of C–H and C–C bonds. During electrocatalytic processes, the breaking of the O=C=O bond requires a high activation energy. In addition, since ECR consists of multiple elementary steps, these electrocatalytic processes are more demanding

than, for example, water-splitting reactions. As ECR reactions are normally carried out in aqueous solutions, another critical issue is the low solubility of CO_2 in water, which impedes the diffusion-controlled reactions. There are certain ways to improve CO_2 dissolution, including using nonaqueous electrolytes and increasing CO_2 partial pressure. For instance, some metal catalysts with low activity for ECR under atmospheric pressure, however, can reduce CO_2 to CO and HCOOH efficiently at high pressures [58].

Electrocatalysts can effectively reduce activation energy, accelerate reactions or increase desired product selectivity in ECR. It should also dissociate water in solution to promote proton–electron transfer because the proton-assisted multiple-electron transfer can be beneficial for CO_2 activation. Depending on the different pathways and the number of protons and electrons transferred, a range of products can be formed, including C_1 products, such as carbon monoxide (CO), methanol (CH_3OH), formic acid (HCOOH), methane (CH_4), or C_2 products, such as ethylene (C_2H_4), ethanol (C_2H_5OH) and others [59]. C_2 products with higher energy densities are more valuable, but the synthesis of C_2 products is more difficult than that of C_1 products because of larger numbers of required protons during conversion. Meanwhile, high formation energy of the C–C bonds can decrease the efficiency of the reaction. To achieve specific product selectivity, the design and synthesis of high-performance ECR electrocatalysts is essential.

2.2. Single-Electron vs. Proton-Coupled Electron Reactions

Research on ECR has been conducted ever since the early 19th century. ECR contains two half reactions occurring in the anode and the cathode, where different numbers of proton-coupled electron transfers occur. The standard electrode potentials of different reactions with reference to standard hydrogen electrons (SHEs) for different products in aqueous solutions are summarized in Table 1. For a typical single-electron ECR, CO_2 is reduced to the CO_2 anion radical (CO_2^-) at the cathode and water is oxidized to oxygen at the anode. Since the kinetics of the reactions are quite sluggish, the first step for converting CO_2 into reduced carbon species is difficult. The thermodynamic potential for driving single-electron CO_2 reduction to CO_2^- is about -1.90 V vs. SHE at a PH of 7, indicating that this reaction is highly energetic and unfavorable [60–62]. In addition, this first step is also the rate-limiting step, and the generation of the CO_2^- intermediate plays a significant role in forming $2e^-$ reduction products. Interestingly, a more favorable route that bypasses the formation of CO_2^- by proton-coupled electron transfer processes has been identified. The transfer of proton-coupled electrons benefits ECR within the potential range of -0.20 to -0.60 V vs. SHE, and the final products are determined by the choices of electrocatalysts and electrolytes as well as the numbers of electrons and protons transferred [63,64]. For instance, two-proton-coupled electron transfer in a CO_2 hydrogenation reaction mainly produces HCOOH and CO.

Table 1. Standard electrochemical potentials for reducing CO_2 into different products.

CO_2 Reduction Reactions	Standard Electrode Potentials vs. SHE (V)
$CO_2 + e^- \rightarrow CO_2^-$	-1.900
$CO2 + 2H^+ + 2e^- \rightarrow HCOOH$	-0.610
$CO2 + 2H^+ + 2e^- \rightarrow CO + H_2O$	-0.530
$2CO_2 + 2H^+ + 2e^- \rightarrow H_2C_2O_4$	-0.913
$CO_2 + 4H^+ + 4e^- \rightarrow HCHO + H_2O$	-0.480
$CO_2 + 6H^+ + 6e^- \rightarrow CH_3OH + H_2O$	-0.380
$CO_2 + 8H^+ + 8e^- \rightarrow CH_4 + 2H_2O$	-0.240
$2CO_2 + 12H^+ + 12e^- \rightarrow C_2H_4 + 4H_2O$	-0.349
$2CO_2 + 12H^+ + 12e^- \rightarrow C_2H_5OH + 3H_2O$	-0.329
$2CO_2 + 14H^+ + 14e^- \rightarrow C_2H_6 + 4H_2O$	-0.270
$3CO_2 + 18H^+ + 18e^- \rightarrow C_3H_7OH + 5H_2O$	-0.310

As shown in Figure 1, ECR starts by transferring a proton–electron pair to form carboxyl (*COOH) or formate (*OCHO) intermediate species [53]. These two intermediates

can be further reduced by accepting different numbers of proton–electron pairs. Note that there is much competition between intermediate species. For example, the OHCO* species can be converted to HCOOH, and the biformate (H_2COO*) can also be reduced to HCOOH. Meanwhile, the different products also show similar reduction potentials. Thus, further reactions of these intermediate species are important for the reaction rate and formation of the final products. Moreover, as the equilibrium potential of a hydrogen evolution reaction (HER) (0 V vs. reversible hydrogen electrode (RHE)) is more positive than that of CO_2 reduction to HCOOH (-0.17 V vs. RHE), H_2 will be the by-product, which seriously limits ECR efficiency [65].
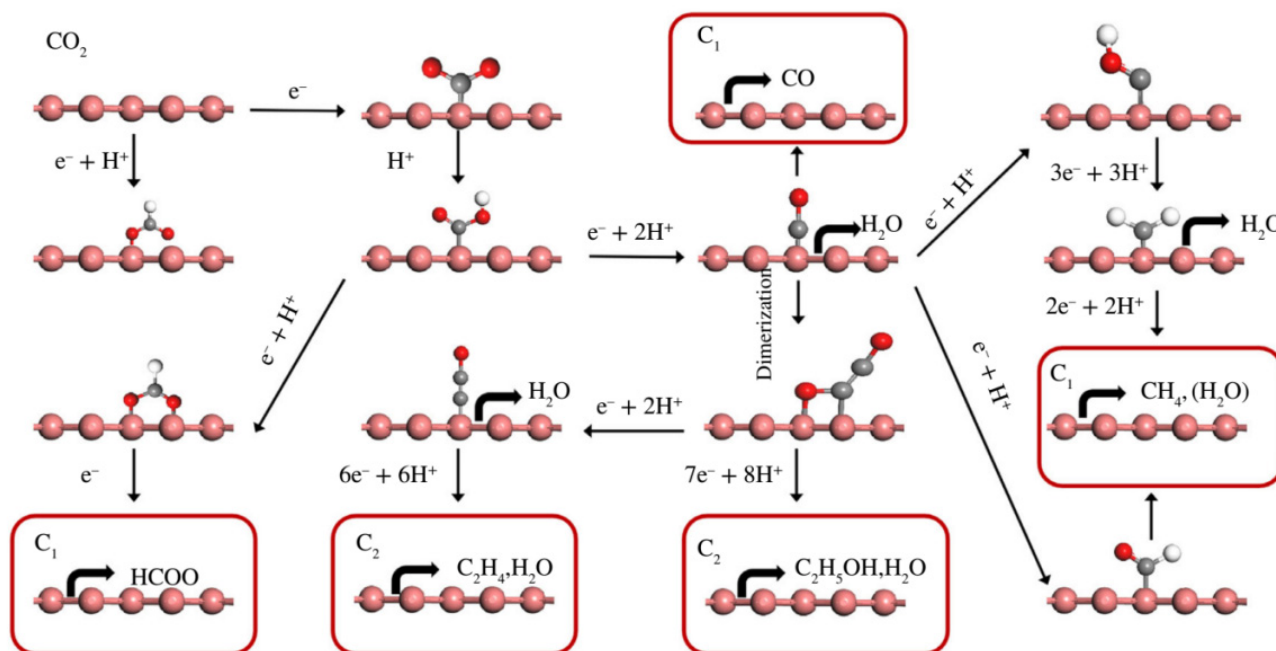

Figure 1. Potential electrochemical CO_2 reduction pathways to form the C_1 products CO, HCOOH and CH_4 and the C_2 products C_2H_4 and C_2H_5OH. Reprinted from [53], Copyright (2019), with permission from Wiley.

2.3. Factors Determining Product Selectivity

Factors such as the type of electrocatalyst (morphology, composition, chemical state and crystallographic structure), type of electrolyte (composition, concentration and pH), temperature, pressure and applied potential all influence ECR. For instance, solid and aqueous electrolytes have been used in ECR, exhibiting remarkable differences in efficiency [66,67]. To date, $NaHCO_3$ and $KHCO_3$ solutions are frequently chosen as electrolytes because they can maintain the pH at the electrode surface. Meanwhile, the pH of the solution can affect the generation of by-products such as H_2.

ECR, with a more positive potential vs. SHE, is thermodynamically more favourable. In this regard, the conversion of CO_2 to alcohol or hydrocarbon products should be thermodynamically more favourable than to other products, including CO, HCOOH and HCHO (Table 1). Nevertheless, ECR not only needs to overcome the thermodynamic barrier but also the kinetic challenge determined by the concentration of available protons in reaction. Namely, the electrocatalysts prefer to transfer electrons from their catalytic sites to adjacent sites which can provide protons. Thus, the formation of hydrogenated C_1 intermediates such as HCOOH can be kinetically more favourable than the formation of C–C bonds, which hinders the selectivity to C_2 and higher hydrocarbon products. To date, only the Faradaic efficiency (FE) of C_1 products CO and HCOOH can reach 100%, while the maximum FE of C_2 product C_2H_4 is 80% and the maximum FE of C_3 product C_3H_7OH is 30% [68,69].

Many theoretical studies proposed that for multielectron transfer reduction of CO_2, the adsorption energies of intermediates follow linear scaling relationships, and breaking such linear scaling relationships can improve catalytic performance. Some strategies have been proposed, including reducing coordination numbers, doping with *p*-block elements, engineering oxyphilic sites and coating the catalyst surface with active ligands. Up to now, the majority of the ECR electrocatalysts have been metal- and carbon-based materials. It has been demonstrated that some heterogeneous electrocatalysts follow the two-electron-transfer mechanisms in CO_2 reduction to HCOOH or CO. For example, Hori et al. investigated a series of metals for ECR reaction and indicated that metallic electrocatalysts, such as Cd, Sn, Hg and Pb, prefer HCOOH formation [70]. However, noble metals, including Pt, Ag and Au, can convert CO_2 into CO. Copper-based electrocatalysts are the only electrocatalysts that have been reported for converting CO_2 into alcohols and hydrocarbons with good activity and selectivity. However, as mentioned above, the interaction between intermediates and electrocatalysts plays a crucial role in forming final products, demonstrating the importance of electrocatalysts.

2.4. Key Parameters for Evaluating ECR Efficiency

In experimental ECR study, there are several key parameters for evaluating electrocatalyst performance, including overpotential, current density, Tafel slope, FE, turnover frequency (TOF) and stability of electrocatalysts. The overpotential can be regarded as the energy needed to drive the reaction. In other words, the higher the overpotential, the higher the energy required for the reaction and the more difficult the reaction to be realized. Current density reflects the rate of electrochemical reaction, and the larger the current density, the faster the electrocatalytic reaction. The Tafel slope can be obtained by fitting the linear region of the Tafel curve. With the increase in overpotential, if the current density increases dramatically, the slope will be small. FE is regarded as the fraction between charges transferred to specific products and the total charges in the electrocatalytic process, accounting for the selectivity and efficiency of the reaction. Larger FE suggests less energy loss, and smaller FE indicates more energy loss. TOF is the catalytic activity of each site under a certain overpotential, indicating the intrinsic activity of catalysts. The stability of electrocatalysts can be evaluated by long-term use under a specific voltage.

In summary, the electrocatalytic reaction is a complicated multistep reaction occurring at the multiphase interface. Small overpotential and high current density can boost ECR, but it is difficult to satisfy them simultaneously. Developing excellent electrocatalysts to overcome these problems is the key.

3. Two-Dimensional Materials as Efficient ECR Electrocatalysts

Compared to bulk materials, 2D materials have a disordered state in their normal direction and a long-range order in the plane, showing a sheet structure. In addition, 2D materials can be exfoliated to single- or multiple-atom thickness, exhibiting interatomic covalent bonds in the plane. The physicochemical properties of 2D materials are different from that of bulk materials. The high atomic exposure rate, large specific surface area and flexible structure make them promising ECR catalysts. Some reported 2D-materials-based electrocatalysts for ECR are summarized in Table 2 and are illustrated in detail in the following sections. Many metals (Ag, Cu, Au, Pt, Pd, etc.), graphene-based materials, Ni/Fe/Zn-doped nitric carbide, metal-doped TMDs and MOFs can produce CO. Particularly, single TM atoms embedded in 2D materials as SACs can exhibit great CO selectivity. Metal oxides and graphene-based materials can produce HCOOH. Interestingly, only Cu-based materials can produce CH_4, C_2H_4 and other C^{2+} products.

Table 2. Typical electrocatalysts in ECR.

Electrocatalyst	Product	FE (%)	Potential	Reference
Pd-Pt/C	HCOOH	88	−0.40 V vs. RHE	[16]
nanoporous silver	CO	92	−0.50 V vs. RHE	[30]
copper foam	CO	80	−1.00 V vs. Ag/AgCl	[66]
Cu-Al	C_2H_4	80	−1.50 V vs. RHE	[68]
GN/ZnO/Cu_2O	C_3H_7OH	30	−0.90 V vs. Ag/AgCl.	[69]
graphene-supported MoS_x	CO	85.1	−0.65 V vs. RHE	[71]
Au NW	CO	94	−0.35 V vs. RHE	[72]
ultrathin Pd nanosheets	CO	94	−0.50 V vs. RHE	[73]
Pd-Au	CO	80	−0.50 V vs. RHE	[74]
nitrogen-doped 3D graphene foam	CO	85	−0.58 V vs. RHE	[75]
ultrathin Bi	HCOOH	86	−1.10 V vs. RHE	[76]
ultrathin porous Cu nanosheets	CO	74.1	−1.00 V vs. RHE	[77]
Cu nanocubes	C_2H_4	60	−0.50 V vs. RHE	[78]
B-doped graphene	HCOOH	66	−1.40 V vs. SCE	[79]
N-doped graphene	HCOOH	73	−0.84 vs. RHE	[38]
N-doped graphene quantum dots	$C_2H_5OH + C_2H_4$	45	−0.75 V vs. RHE	[59]
Au NPs x-embedded graphene nanoribbon	CO	92	−0.66 V vs. RHE	[80]
Ni-N modified graphene	CO	90	−0.70 V vs. RHE	[81]
N-doped graphene monolayer-coated Sn foil	HCOOH	92	−1.00 V vs. RHE	[82]
Sn quantum sheets confined in graphene	HCOOH	86	−1.80 V vs. SCE	[83]
SnS_2 supported on graphene oxide	HCOOH	84.5	−1.40 V vs. Ag/AgCl	[84]
g–C_3N_4/MWCNTs	CO	60	−0.75 V vs. RHE	[85]
Co_3O_4-CDots-C_3N_4	CO	89	−0.60 V vs. RHE	[86]
Nb-doped vertically aligned MoS_2	CO	82	−0.80 V vs. RHE	[87]
MoS_2	CO	98	−0.764 V vs. RHE	[88]
WSe_2 nanoflake	CO	24	−0.164 V vs. RHE	[89]
Cobalt–porphyrin MOF	CO	76	−0.70 V vs. RHE	[90]
Zn MOF	CO	71.9	−0.89 V vs. RHE	[91]
Co-based phthalocyanine	CO	99	−0.80 V vs. RHE	[92]
ultrathin Co_3O_4	HCOOH	64.3	−0.88 V vs. SCE	[93]
oxygen-deficient Co_3O_4	HCOOH	87.6	−0.87 V vs. SCE	[94]
atomic Co_3O_4	HCOOH	90	−0.85 V vs. SCE	[28]
mesoporous SnO_2 nanosheets	HCOOH	87	−1.60 V vs. Ag/AgCl	[95]
Cu-CeO_2	CH_4	58	−1.80 V vs. RHE	[96]
Fe–N_4–C	CO	80	−0.50 V vs. RHE	[97]
Fe–N_4–C	CO	80	−0.57 V vs. RHE	[98]
Fe–N_5–C	CO	97	−0.46 V vs. RHE	[99]
Fe–N_4–C	CO	94.9	−0.5 V vs. RHE	[100]
Fe^{3+}–N–C	CO	90	−0.45 V vs. RHE	[101]
Zn–N–C	CO	95	−0.43 V vs. RHE	[102]
Ni-graphene oxide	CO	96.5	−0.63 V vs. RHE	[103]
Ni(I)–N_4–C	CO	97	−0.61 V vs. RHE	[104]
Ni–N_4–C	CO	90	−0.65 V vs. RHE	[105]
Ni–N_2–C	CO	98	−0.80 V vs. RHE	[106]
STPyP–Co	CO	96	−0.62 V vs. RHE	[107]
Cu–N_2/GN nanosheets	CO	81	−0.50 V vs. RHE	[108]

3.1. Two-Dimensional Metallic Materials

　　Bulk metal catalysts in ECR have been investigated for decades [109–111]. Metal electrocatalysts can be divided into two groups: noble metal (Au, Ag, Pt, etc.) and other earth-abundant transition metals (Co, Ni, Cu, etc.). Theoretical work has well disclosed that noble metals are better electrocatalysts compared with earth-abundant metals. Nevertheless, some intermediates, such as CO, could poison the active sites, which affects their stability. Large-scale application of precious metals is also not possible due to their high price and scarcity.

　　It has been revealed that precious metals with 2D nanosheet structures can enhance their electrocatalytic performance effectively and improve the utilization of noble

metals [72]. Huang et al. prepared a hexagonal Pd structure with 2.5 times higher electro-catalytic activity for the oxidation of formic acid compared to commercial Pd black [112]. The high performance could be attributed to nanosheet structure with more active sites, better electronic structure and larger surface area, as well as high atom utilization. Zhu et al. synthesized ultrathin Pd nanosheets for ECR, which exhibited an FE of 94% for CO production at a potential of -0.50 V vs. RHE [73]. Meanwhile, experimental and theoretical work revealed that ultrathin Pd nanosheets with high edge exposure ratios are beneficial for CO_2 adsorption and CO desorption as well as suppressing HER. Nanostructured Au also shows great activity in ECR. Mistry et al. studied the electrocatalytic activity of Au nanoparticles (NPs) in the range of 1–8 nm for CO_2 reduction to CO [113]. The results suggested that the current density increases with the decrease in particle size.

Moreover, multimetal composite nanosheets also exhibit excellent performance in electrocatalytic reactions because of the synergistic effect of different metals compared to single-metal electrocatalysts [114–116]. Wang et al. showed that a 2D Pd–Au bimetallic catalyst has lower activation energy than monometallic Au in ECR via density functional theory (DFT) calculation [74]. Very recently, Au–Cu bimetallic thin films with various ratios were synthesized for ECR [117]. The activity of the Au–Cu alloy was found to be correlated with the variation of electronic structures determined by alloy composition. As shown in Figure 2a, the surface valence bands of the Au–Cu catalysts present different patterns with different alloy compositions. The *d*-band center gradually moves away from the Fermi level with the increase in Au concentration (Figure 2b), which could influence the occupancy of antibonding states. Meanwhile, the interaction strength between substrate and intermediates decreases. The *d*-band center does not shift after ECR, implying great stability. Therefore, the catalytic performance for CO formation is enhanced as Au concentration increases, with the highest current density and FE at -0.80 V vs. RHE (Figure 2c,d).
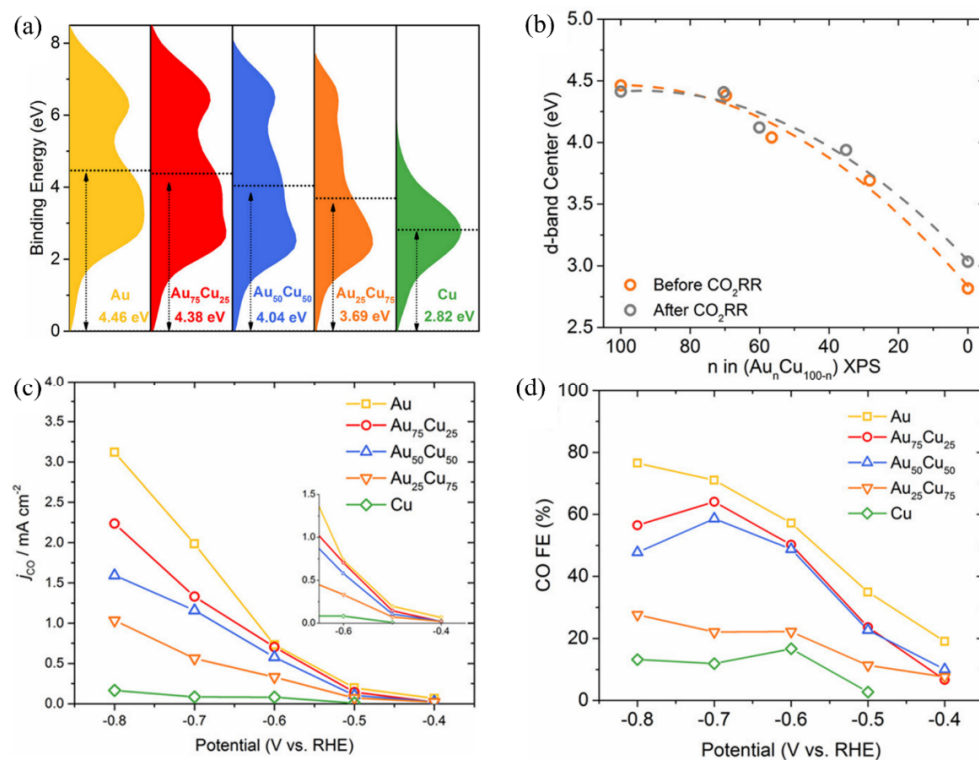

Figure 2. (**a**) Surface valence band X-ray photoemission spectra of the as-prepared Au, Cu and Au–Cu alloys. (**b**) *d*-band center of different samples before and after ECR at -0.7 V vs. RHE for 1 h. The gravity center of the valance band center is shown by the dotted lines compared to 0 eV. The binding energy is the value of $|E - E_{Fermi}|$. (**c**) Faradaic efficiency of and (**d**) partial current densities of CO. Reprinted from [117], Copyright (2018), with permission from American Chemical Society.

Nonprecious metals, including Fe, Co, Ni, etc., have also attracted much attention in electrocatalysis due to low prices, abundant resources and promising electrochemical properties as well as tunable electronic structures [118,119]. Studies have shown that Fe, Ni and Ti produce H_2 as the major product in ECR due to their low HER overpotential and strong CO adsorption capability. Sn, Pb and In have poor binding energy with CO_2^- intermediates and the final products are usually formate or formic acid. Moreover, Cu is the only metal catalyst that can produce C_3 hydrocarbons by a C–C coupling mechanism [120]. Generally, modulating the electronic and surface structures of these metals could effectively enhance their electrocatalytic activity. Kuang et al. synthesized ultrathin Ni nanosheet arrays by an in situ topology reduction technique. In their study, the electrocatalyst showed excellent HER activity compared with Pt/C because ultrathin nanosheet structure could expose more active sites which boost electrocatalytic reactions [121]. In addition, 2D-structured bismuth (Bi) exhibited more active sites and promising selectivity to formate compared to bulk Bi. Zhang et al. prepared ultrathin Bi by a liquid phase stripping technique. The ultrathin Bi displayed excellent electrocatalytic performance for formate generation with an FE of 86% and a current density of 16.5 mA/cm^2 at −1.1 V vs. RHE, which is obviously higher than bulk Bi and acetylene black decorated carbon paper (AB/CP) (Figure 3a,b). As presented in Figure 3c,d, CO_2 conversion to HCOOH underwent lower Gibbs free energy change on edges (003) and (012) [76]. Special surface structure can also improve the catalytic efficiency and selectivity. It has been reported that ultrathin porous Cu nanosheets synthesized by a simple replacement method can achieve an FE of 74.1% and current density of 23.0 mA/cm^2 at −1.0 V vs. RHE for CO_2 conversion to CO, remarkably better than that of traditional bulk Cu [77]. DFT calculations clarified that the porous Cu nanosheet structure can accelerate the formation of CO intermediate, thus promoting ECR efficiency. Similarly, Wang et al. synthesized Cu nanocubes which demonstrated better electrocatalytic activity and selectivity in comparison with Cu nanospheres of the same size. The nanocubes could reach an FE of 60% and a partial current density of 144 mA/cm^2 towards C_2H_4 production [78]. Zhang et al. prepared the pipet-like bismuth (Bi) nanorods semifilled in nitrogen-doped carbon nanotubes (BiNRs@NCNTs) for ECR [122]. The catalyst acted as a nanoscale conveyor which could facilitate mass transport and reactant adsorption on active sites. As a result, the FE for formate generation reached 90.9% at a moderate applied potential of −0.9 V (vs. RHE).

Therefore, metal catalysts are effective for electrocatalysis due to their intrinsic activity and good conductivity. When the metal catalysts are synthesized with 2D nanosheets or other special nanostructures, the atom utilization, activity and selectivity could be improved, thus increasing electrocatalytic efficiency. Precious metals, such as Pd or Au, or multimetals with different ratios show excellent selectivity for CO generation. Nonprecious metals, such as Fe, Co and Ni, show poor ECR performance, while Sn, Pb and In can have good activity for the production of formate or formic acid. Particularly, Cu-based catalysts with different morphologies can exbibit different activities and selectivities for different products. Accordingly, the choice of metal, small nanosheet size and different morphology will have a positive effect on ECR activity and selectivity.

3.2. Graphene and Graphene-Based Materials

Generally, graphene is a single layer of graphite with a zero-band gap. It is a promising electrocatalyst for CO_2 reduction due to its high electron mobility, conductivity, unique electronic structure and large surface area. In addition, the high thermal conductivity can improve heat diffusion during the exothermic process, benefiting electrocatalysis. However, pristine graphene exhibits some drawbacks in ECR. For instance, the delocalized π bonding network of graphene negatively affects the adsorption of intermediates such as *COOH or *OCHO; therefore, graphene cannot effectively activate the CO_2 molecule and presents high-energy barriers for intermediate formation, leading to low ECR activity [123]. Some studies have clarified that the undoped zigzag edge of graphene shows a metastable adsorbed CO_2 state, and the energy barrier is quite high at about 1.3 eV [124]. As the

modification of electronic structures can efficiently tackle these problems, many researchers have focused on tailing its electronic structures. For example, incorporating heteroatoms, such as B or N, can effectively modify graphene structures and decrease the CO_2 adsorption barrier. Studies have disclosed that N-doped graphene can exhibit a low overpotential of around 0.19 V for converting CO_2 into CO [75]. Duan et al. reported that doping boron can stabilize the negatively polarized O atoms of CO_2 and improve CO_2 chemisorption on carbon surfaces [125]. Similarly, Sreekanth et al. reported B-doped graphene as a metal-free electrocatalyst for CO_2 reduction in 0.1 M $KHCO_3$ solutions. They concluded that the presence of boron dopants can introduce spin density distribution and these atoms can be active sites for intermediate adsorption [79]. Some doped systems have been investigated in more detail by DFT calculations. Wu and coworkers systematically studied the effect of N-doped graphene for ECR. Three different N atom sites, including graphitic N, pyrrolic N and pyridinic N, were investigated as active sites for ECR. The authors suggested that the three different N sites can significantly decrease the free energy barrier for intermediate adsorption. The triple-pyridinic N can most effectively reduce the barrier for COOH adsorption, indicating that pyridinic N is a highly active site for converting CO_2 to CO [75]. However, there are different views on the mechanism of N-doped graphene for ECR. Chai et al. reported that the graphitic N-doped edges of graphene sites have low CO_2 activation barriers and are the most active sites for ECR among graphene-based materials [124]. Liu et al. demonstrated that a pyrrolic N site performs the best for CO_2 reduction to HCOOH with a low overpotential [126]. It has also been reported that N-doped graphene quantum dots with predominant pyridinic N at the edges can electrochemically convert CO_2 to C_2 compounds with low overpotentials [59].
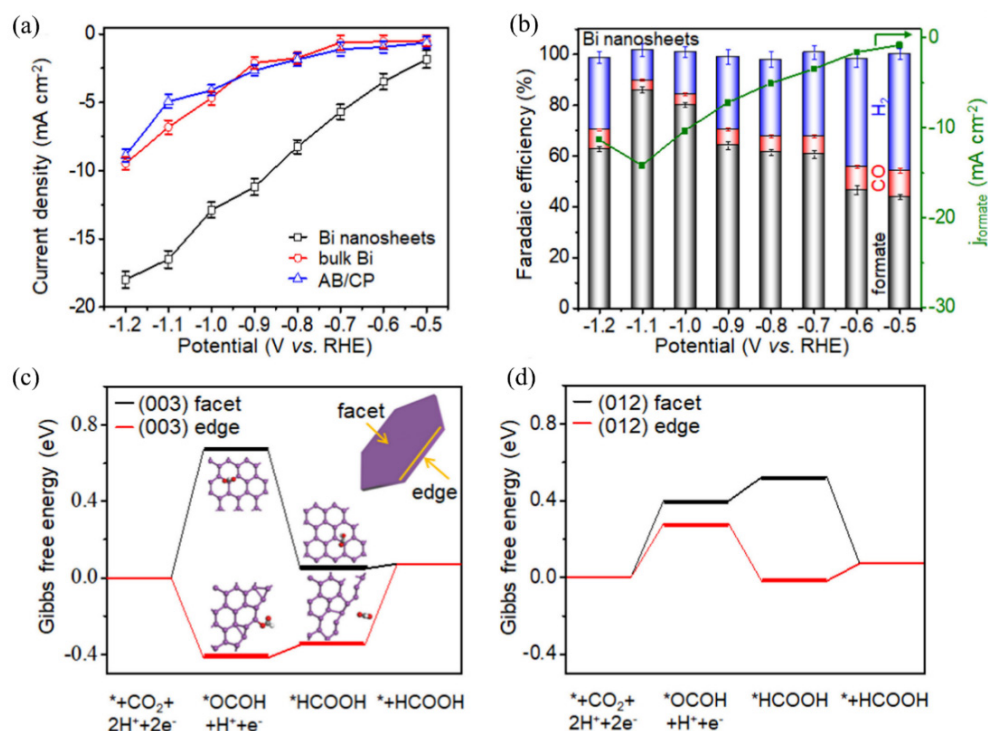

Figure 3. (**a**) Current densities of Bi nanosheets, bulk Bi and acetylene black decorated carbon paper (AB/CP) within a potential window of −0.5 to −1.2 V vs. RHE in CO_2-saturated 0.1 M $KHCO_3$ aqueous solution. (**b**) Faradaic efficiencies (left Y axes) and partial current densities of formate product (right Y axes) of Bi nanosheets. DFT calculated ΔG in the reaction pathways of CO_2 conversion to formate from the facet sites and edge sites of the (**c**) (003) plane and (**d**) (012) plane on Bi. Reprinted from [76], Copyright (2018), with permission from Elsevier.

Compared with nonmetal dopants, introducing single or multiple metal dopants to construct special graphene nanostructures could also exploit materials with excellent catalytic performance. Au nanoparticles embedded in graphene nanoribbon exhibit low overpotential, high FE for CO generation and excellent stability compared to amorphous carbon-supported Au nanoparticles, attributed to the change in electronic properties and the increase in active sites [127]. Liu et al. synthesized Pd and Cu mono- and bimetallic nanoparticle-embedded graphene and suggested that 1 wt.% Pd–2 wt.% Cu/graphene had the highest ECR efficiency [80]. Su et al. prepared nickel–nitrogen comodified graphene (Ni–N–Gr) with more active centers by short-duration heat treatment and found that the Ni–N site was the active center for CO_2 reduction [81]. As shown Figure 4a,c, the Ni–N–Gr and the Ni foil exhibit obvious enhancement of current density in the presence of CO_2. However, there is a remarkable difference in FE of CO. The Ni–N–Gr showed an FE of 90% at -0.7 to -0.9 V vs. RHE for CO production, where Ni foil produced mostly H_2 (Figure 4b,d), demonstrating that the synergistic effect of Ni and N is critical for improving CO selectivity.
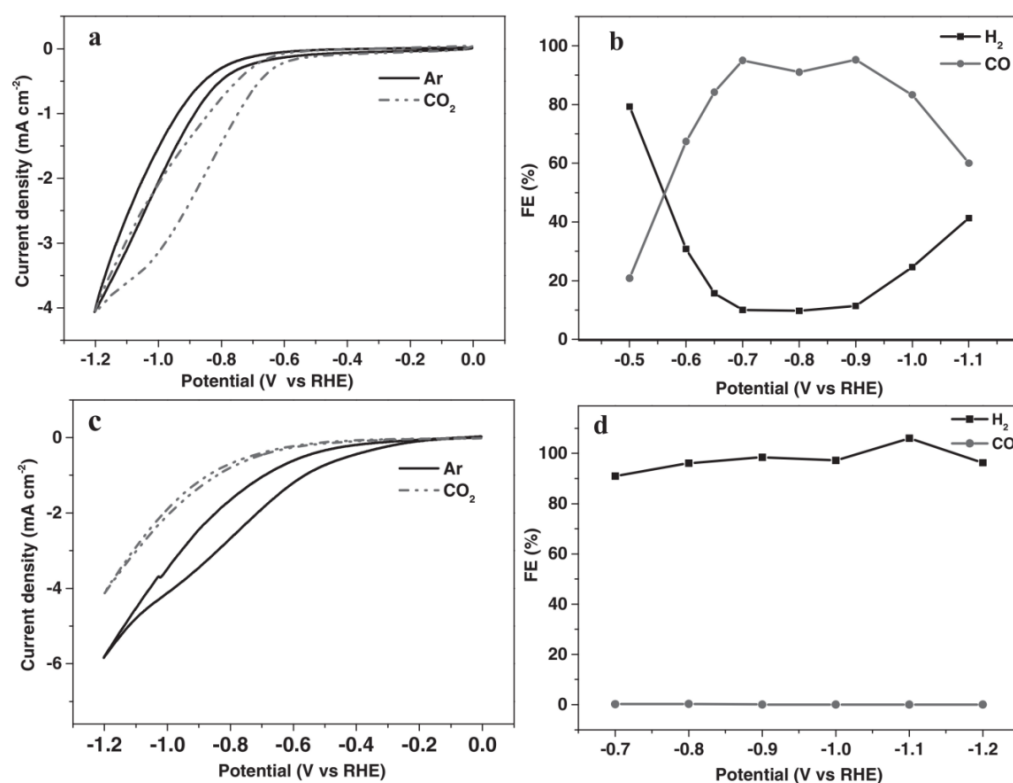

Figure 4. (**a**) Cyclic voltammograms of nickel–nitrogen comodified graphene (Ni–N–Gr) catalyst and (**c**) Ni foil in CO_2-saturated 0.1 M $KHCO_3$ and Ar-saturated 0.1 M KH_2PO_4/K_2HPO_4 (pH = 6.8) at 10 mV s^{-1}. FEs for the reduction products by (**b**) Ni–N–Gr catalyst and (**d**) Ni foil. Reprinted from [81], Copyright (2016), with permission from Wiley.

Graphene-based composite materials also possess excellent conductivities and larger surface areas compared to pristine graphene. Huang et al. synthesized N-doped graphene monolayer-coated Sn foil, showing excellent flexibility with a high FE of 92% for formate at -1.0 V vs. RHE [82]. Lei et al. prepared Sn quantum sheets confined in graphene, offering more active sites for CO_2 adsorption [83]. Li et al. successfully prepared SnS_2 nanosheets supported on reduced graphene oxide for CO_2 conversion to formate, displaying a low overpotential of 0.23 V and a maximum Faradaic efficiency of 84.5%. The spectroscopic and electrochemical characterizations suggested that the improvement of electrocatalytic performance can be attributed to the residual SnS_2 [84].

For graphene-like materials, graphitic carbon nitride (g–C_3N_4) typically exhibits good chemical and thermal stability under ambient conditions. However, poor conductivity and less active sites limit its potential application in ECR. Strategies, including doping metal and constructing composite, have been developed to increase the activity of g–C_3N_4. Metal atoms can effectively modulate the electronic structure of g–C_3N_4, thus improving the catalytic activity. The g–C_3N_4 nanosheet and multiwalled carbon nanotubes composite have been shown to exhibit excellent stability and good electrocatalytic performance for CO_2 reduction to CO [85]. The electrocatalytic activity of the composite arises from the C–N bonds, and the high conductivity allows numerous electrons to transfer rapidly to the C–N sites. Guo et al. synthesized Co_3O_4–CDots–g–C_3N_4 tricomponent electrocatalysts for syngas production [86]. They suggested that different catalytic components have different functionalities. For instance, g–C_3N_4 and Co_3O_4 provide active sites for ECR and HER, respectively, whereas CDots are the sites for proton generation.

It can be concluded that the electronic structure of graphene-based materials can be tuned to effectively improve ECR selectivity. Doping nonmetal or metal atoms is an efficient way for the design and synthesis of high-performance ECR catalysts. To date, nitrogen and metal atom codoping has been widely reported and shown excellent activity for CO production. Constructing highly active interfaces in graphene-based nanocomposite is also a good strategy in ECR catalyst design.

3.3. Two-Dimensional Transition Metal Dichalcogenides

Transition metal dichalcogenides (TMDs), such as MoS_2, $MoSe_2$ and WS_2, have the general formula MX_2, where M is a transition metal atom and X represents a chalcogen atom. The layers of X–M–X are stacked together by the van der Waals interaction. This is another class of 2D materials with exceptional physical and chemical properties to be applied as electrocatalysts [88]. The large surface area of 2D TMDs can provide more active sites for reactions such as CO_2 reduction and water splitting [128,129]. DFT calculations suggested that the excellent catalytic properties for metal-terminated edges of 2D TMDs can be attributed to its metallic character and high *d*-electron density [87]. It has been confirmed that intermediates, such as COOH and CHO, prefer to adsorb on MoS_2 and $MoSe_2$ edges than the bridge S or Se atoms, and CO species adsorb selectively on the metal atoms during ECR [130,131]. Four different TMD materials, MoS_2, $MoSe_2$, WS_2 and WSe_2, have been investigated as ECR catalysts; of which, WSe_2 nanoflakes exhibit the highest activity at an overpotential of 65 mV with an exceptional current density of 330 mA/cm^2 and an FE of 85% for CO generation, surpassing other electrocatalysts [89]. The excellent performance can be attributed to WSe_2 nanoflakes' much lower charge transfer resistance and low work function. DFT calculations showed that the formation of CO is kinetically favorable.

Further efforts have been made to enhance intrinsic activity, suppress the competing HER reaction and improve catalyst stability. It has been reported that doping and alloying different metal atoms with TMDs could enhance electrocatalytic efficiency by tuning the binding strengths of reaction intermediates and the reaction energy barrier. For instance, in one study, 5% niobium (Nb)-doped vertically aligned MoS_2 showed the largest CO_2 reduction current density of ca. 237 mA/cm^2 at the potential of −0.80 V, which was about two to three times higher than that of pristine and Ta-doped MoS_2 (Figure 5a). Nb-doped MoS_2 displayed an order of magnitude higher TOF for CO generation than pure MoS_2 at an overpotential of 20–150 mV and two orders of magnitude higher TOF for CO formation than Ag nanoparticles at the potential range of 0–650 mV (Figure 5b). The Nb atom could facilitate rapid CO release from the TMD edge, which remarkably increased ECR efficiency [87]. Theoretical calculation elucidated that there is a linear scaling relationship between the adsorption energies of the crucial intermediates, including COOH*, *CHO and *CO. It means that the stabilities of these intermediates are closely related, which causes a persistent overpotential for ECR. Theoretically, to improve ECR activity, breaking the linear scaling relationship between the binding energies of intermediates would be a good solution. Norskøv et al. have revealed that if the intermediates bind to different active sites,

the linear scaling relation can be broken at the edge site of MoS_2 and $MoSe_2$, which can increase ECR activity. They further showed that the doped S edge of MoS_2 can meet this requirement with *CO bonding on the doped metal atoms and *COH, *CHO and *COOH binding on the S sites [130]. Therefore, the binding energies of these three intermediates are higher than that of CO*, suggesting the breaking of the linear scaling relationship.
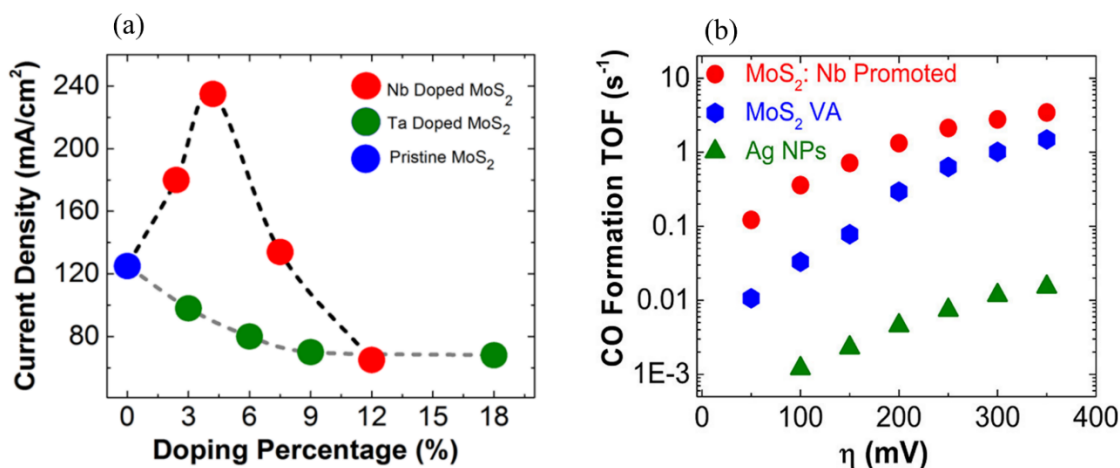

Figure 5. (**a**) Current density as a function of dopant percentage for Nb doped and Ta doped MoS_2 samples. (**b**) Calculated CO formation TOF at different applied overpotentials for 0.5% Nb-doped MoS_2, pristine VA-MoS_2 and Ag nanoparticles. Reprinted from [87], Copyright (2017), with permission from American Chemical Society.

Among four different TMD materials, MoS_2, $MoSe_2$, WS_2 and WSe_2, WSe_2 exhibits good CO selectivity because of its lower work function and charge transfer resistance. Metal doping is also an effective way to improve ECR performance of TMD materials. More importantly, breaking the linear scaling relationship between the binding energies of intermediates will be a good strategy for designing excellent TMD catalysts.

3.4. MOF Materials

MOFs are a new type of porous material with metal ions or clusters coordinated with organic ligands. Due to their high porosity, large specific surface area and flexible structure, MOFs have been applied in electrocatalytic research recently [43,132]. However, some disadvantages, such as poor conductivity and less active centers, hamper their electrocatalytic activity. Studies have shown that low-dimensional MOFs can achieve high electrocatalytic performance because MOF nanosheets can expose more active atoms and exhibit excellent electron transfer. Moreover, the metal atoms, ligand and the connection of metal centers with ligands also play vital roles in the electrocatalytic activity of MOFs. Kornienko et al. synthesized a thin film cobalt–porphyrin MOF on a carbon substrate. The FE of this sample was 76% at −0.70 V vs. RHE for CO_2 conversion to CO. In addition, it possessed a low Tafel slope of 165 mV/decade and the electrocatalytic stability was excellent [90]. A Zn MOF synthesized by ionic exchange of Zn nodes with adsorbed Ni salts achieved an FE of 71.9% for CO at 10.48 mA/cm^2 under the potential of −0.89V vs. RHE [91]. Zhang et al. prepared a series of transition-metal-based MOF electrocatalysts by using phthalocyanine (Pc), which can convert CO_2 to CO efficiently [92]. Under controlled potential electrolysis tests of different samples in CO_2-saturated solution, the Co-based MOF exhibited the lowest onset potential and largest current density (Figure 6a). Remarkably, Co-based MOF also showed the largest CO current density in a wide potential range (Figure 6b). Moreover, Co-based MOF exhibited 99% FE of CO formation under the potential of −0.80 V, as shown in Figure 6c,d, demonstrating that Co-based MOF is the best catalyst for CO_2 conversion to CO among others. DFT calculations suggested that the rate-limiting step for CO_2 conversion to CO had the lowest Gibbs energy change (Figure 6e). As shown in the inset of Figure 6e, the adsorption energy of *COOH on N and C sites was 0.95 and 0.90 eV,

which is much larger than that of −0.1 eV on the Co site, indicating that metal center is the most stable adsorption site. Moreover, two linear relationships disclosed a volcano curve (Figure 6f) in which the location of Co-based MOF is closest to the volcano peak. Therefore, it shows the best intrinsic activity for ECR into CO.
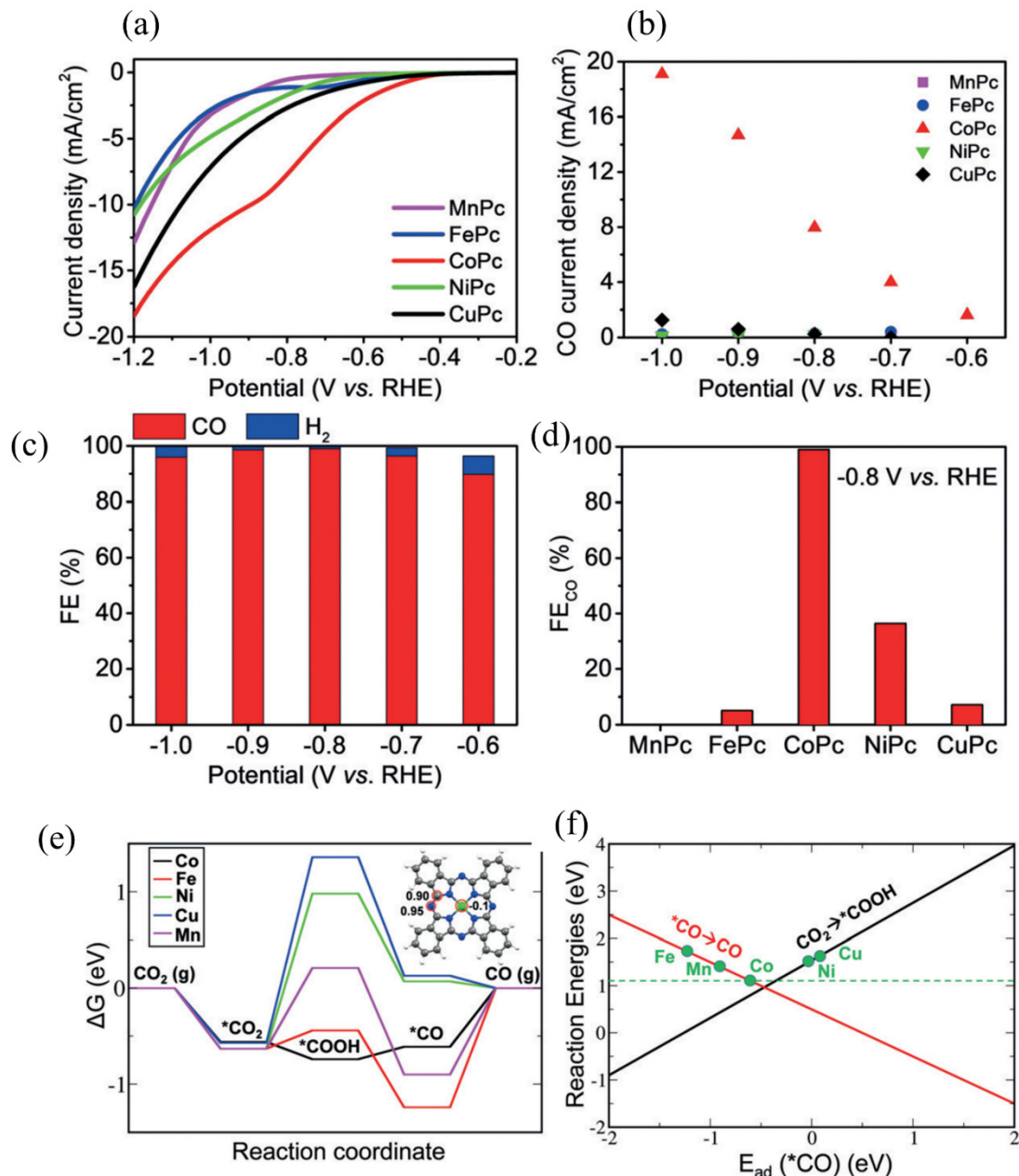

Figure 6. (**a**) Linear-sweep voltametric (LSV) tests in CO_2-saturated electrolyte. (**b**) CO current density of MePcs at various potentials. (**c**) Faradaic efficiency of CO and H_2 formation at different potentials for the CoPc sample. (**d**) Faradaic efficiency of CO formation at −0.8 V versus RHE for the different MePc samples. (**e**) The calculated free-energy diagram for all the MePc electrodes. The inset shows the adsorption energy of *COOH (unit eV) on different sites of CoPC. (**f**) Fitted *CO desorption and *COOH formation trends over the five MePc electrodes. Reprinted from [92], Copyright (2018), with permission from Wiley.

Recently, Perfecto-Irigaray et al. developed Cu-based MOF by doping metals (Zn, Pd and Ru) into HKUST-1 with different ratios [133]. They reported that the Ru-doped sample (10 wt.% Ru) showed an FE of 47.2% for methanol and ethanol generation, while other

metal-doped samples performed worse compared to the pristine HKUST-1. Nevertheless, all doped samples exhibited increased ethanol selectivity. This is ascribed to the formation of C–C bonds on metal sites that boost the formation of C_2 or C_3 intermediates, which are finally converted into alcohol or other high-carbon products. Very recently, 2D copper tetrahydroxyquinone conductive MOF (Cu-THQ) was reported for ECR at a low overpotential. Cu-THQ nanoflakes with an average particle size of 140 nm showed the largest current density of about 173 mA/cm^2 under -0.45 V vs. RHE, an average Faradaic efficiency FE_{CO} of about 91% and a remarkable TOF of 20.82 s^{-1}. Spectroscopic characterization and DFT calculations uncovered the importance of reduced Cu^+ during ECR, which was reversibly oxidized to Cu^{2+} after the reaction [134].

Overall, the metal atoms, ligand and the connection of metal center with ligand of MOF materials can determine electrocatalytic activity. Doping of a different metal to the original MOF materials, on the other hand, could either increase or decrease ECR activity.

3.5. Metal Oxide Nanosheets

Metal/metal oxide composites and oxide-derived metal have also been developed as ECR electrocatalysts with high performance [33,135,136]. Nevertheless, metal oxides still suffer problems such as instability and poor conductivity. It has been demonstrated that low-coordinated surface metal cations can be beneficial for CO_2 adsorption during ECR. First principles calculation revealed that both the density of states (DOS) and the charge density around the conduction band edges can be greatly enhanced [137]. Therefore, faster carrier transport along the 2D ultrathin layer during ECR can be expected. One excellent example is the ultrathin Co_3O_4 layers, with thicknesses of 1.72 nm and 3.51 nm, synthesized by fast-heating treatment [93]. The ultrathin Co_3O_4 layer exhibited higher DOS at the conduction band edges than the bulk structure (Figure 7a,b). Moreover, the charge density of the ultrathin Co_3O_4 layer around the conduction band edge was larger and more delocalized than the bulk Co_3O_4 (Figure 7c,d). These changes can be beneficial for faster carrier transport, thus accelerating ECR. Co_3O_4 layers with 1.72 nm thickness displayed a maximum current density of 0.68 mA/cm^2 and FE of 64.3% for formate production at -0.88 V vs. the saturated calomel electrode (SCE) (Figure 7e,f). Figure 7g indicates that the electrochemically active surface area (ECSA) increased with the decrease in thickness from bulk to 1.72 nm, which clearly evidences the close relationship between structure and activity. The intrinsic activity of Co_3O_4 with 1.72 nm thickness was over 1.5 times higher than the 3.51 nm thick Co_3O_4 layers and 20 times higher than the bulk structure (Figure 7h).

Moreover, the authors elucidated an atomic-level relationship between oxygen vacancies and ECR performance by constructing a model of oxygen vacancies confined in atomic Co_3O_4 single-unit cell layers [94]. DFT calculations uncovered that the main defect was oxygen (II), and X-ray absorption fine structure spectroscopy (XAFS) and X-ray photoelectron spectroscopy (XPS) indicated the distinct oxygen vacancy concentration. CO_2 adsorption isotherms demonstrated that the presence of oxygen (II) vacancy can promote CO_2 adsorption, while DFT calculations verified that oxygen (II) vacancy benefits spontaneous HCOO* desorption and prevents catalyst deactivation. More importantly, oxygen (II) vacancy facilitated the rate-limiting proton transfer step by stabilizing the HCOO* intermediate, which was confirmed by the drop of the activation energy barrier from 0.51 to 0.40 eV. This may also improve ECR kinetics because of the decreases in onset potential from 0.81 to 0.78 V vs. SCE and Tafel slope from 48 to 37mV dec^{-1}. Thus, oxygen (II)-vacancy-rich Co_3O_4 nanosheets (0.84 nm) exhibited a current density of about 2.7 mA/cm^2 with 85% formate selectivity for 40 h, which is promising for an ECR electrocatalyst. The researches further prepared a Co-based nanosheet with a thickness of only four atoms (about 0.84 nm) via solvothermal growth. The partial oxidation of the four-atom-thick Co layer can be formed on its surface by controlling the reaction time [28]. Interestingly, the four-atom-thick Co sheets exhibited great potential in ECR because the thinner 2D structures presented more surface-active sites and higher electrical conductivity. In LSV experiments, the partially oxidized four-atom-thick Co layers displayed a distinct CO_2 reduction peak at -0.85 V

vs. SCE with a current density of 10.59 mA/cm^2. It was a performance enhancement by about 10, 40 and 260 times in comparison with Co four-atom-thick layer without oxidation, oxidized bulk Co and unoxidized bulk Co, respectively. More importantly, the partially oxidized four-atom-thick Co layers showed great stability with a current density of 10 mA/cm^2 over 40 h and a high FE for formate generation of about 90% under a low overpotential of 0.24 V. Such a noticeable improvement can be partly attributed to the increase in ECSA. Another reason is that the partially oxidized four-atom-thick Co layer (atomic Co$_3$O$_4$) further increased their intrinsic activity and selectivity compared with pristine four-atom-thick Co layer.

Zhang's group prepared mesoporous SnO$_2$ nanosheets by a facile combination of hydrothermal reaction and calcination on carbon cloth [95]. As shown in Figure 8a,b, dense SnO$_2$ nanosheets grew uniformly on carbon cloth, and these nanosheets also contained numerous pores. The study showed a high partial current density of about 50 mA/cm^2 at −1.6 V vs. Ag/AgCl, with a high Faradaic efficiency of about 87% for formate generation, which outperformed most gas diffusion electrodes (Figure 8c,d). After electrolysis for 24 h, the current density and FE of formate were still stable (Figure 8e). Moreover, Figure 8f indicates that the current density also remained unchanged after folding or twisting the electrode 10 times. The excellent performance can be attributed to the following factors: Firstly, the SnO$_2$ nanosheet could provide intrinsically active sites for ECR; secondly, the highly porous structure could increase the specific surface area, which facilitated charge and mass transfer during ECR; the third reason is that the robustness of the hierarchical structures ensured high stability of the electrocatalyst during long-term use.

Therefore, metal oxide nanosheets mainly produce formate during ECR. The low-coordinated surface metal cations can be active centers for ECR. Ultrathin metal oxides exhibit higher DOS at the conduction band compared to the bulk structure. The charge density is more delocalized, which benefits the carrier transport. In addition, building oxygen vacancy could also increase ECR performance by improving the reaction kinetics.

3.6. Two-Dimensional Materials Incorporated Single-Atom Catalysts

Single-atom catalysts (SACs) have enormous advantages in electrocatalysis in terms of 100% atom utilization and intriguing electronic structures [138,139]. The traditionally supported nanoparticles or clusters exhibit structural irregularities on the nanoparticle surface. The surface reactivity has a close relationship with surface free energy, and the ratio between fully coordinated surface atoms and the number of vacancies distinguishes the reactivity of atoms with identical chemical compositions but different positions [140–142]. Therefore, the conventional clusters with different surface reactivities can result in poor product selectivity. SACs are different from clusters because the surface free energy is homogeneous and the number of vacancies in the nearest neighbors is the same. Thus, SACs can show good stability and special intrinsic activity [143]. Single-atom catalysts exhibit uniform active sites as ideal catalysts; however, one major challenge for SACs is synthesis because SACs are unstable and can agglomerate quickly due to high surface energy. Furthermore, the supported structures in the neighboring environment increase the heterogeneity of SACs' active sites, and thus uniform activity cannot be easily achieved. However, 2D materials can be utilized as supports to improve the uniformity and performance of SACs in electrocatalytic reactions [144,145]. Studies have evidenced that 2D materials, such as MoS$_2$, graphene and MXene, could stabilize the SACs and maintain their single-atom state [96,146–151]. For instance, Back et al. investigated single transition metal atoms anchored on graphene with single or double vacancies as ECR catalysts by DFT calculations [152]. They suggested that many SACs exhibit high selectivity for ECR over the competitive HER because of favorable adsorption of *COOH or *OCHO over *H on the catalysts (Figure 9). SACs for CH$_3$OH production, Ni and Pt, showed limiting potentials of −0.41 V and −0.27 V, respectively, while Os and Ru systems had the same limiting potential (−0.52 V) for CH$_4$ production. The activity improvement of SACs can be partially attributed to the unique electronic structure of the SACs and orbital interaction.
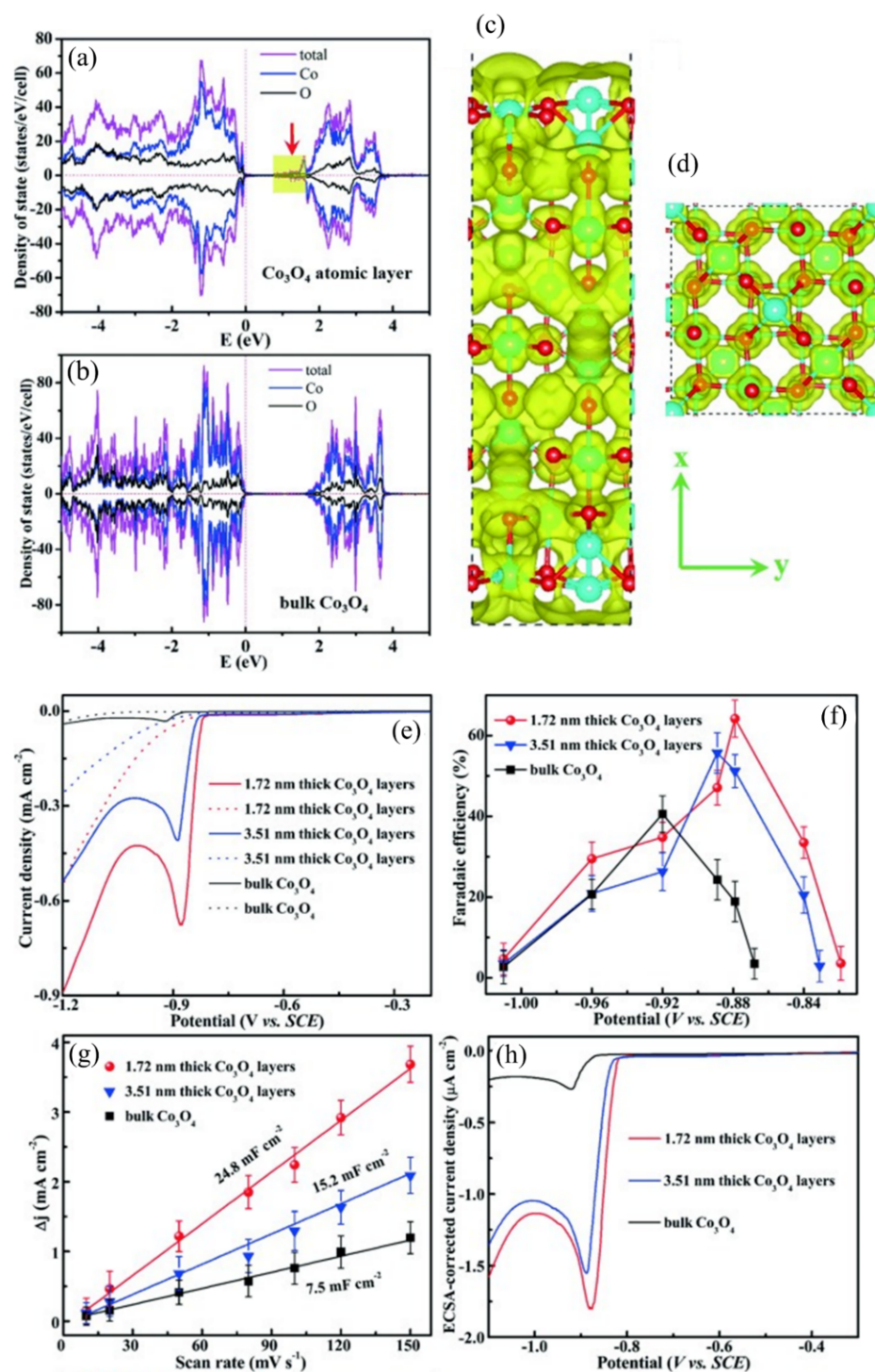
Figure 7. The calculated DOS for (**a**) Co_3O_4 atomic layer slab with a thickness of 1.72 nm and (**b**) bulk Co_3O_4 slab. The yellow shaded parts represent the increased DOS at the conduction band edges of Co_3O_4 atomic layer. The partial charge density around the conduction band minimum of (**c**) Co_3O_4 atomic layer slab and (**d**) bulk Co_3O_4 slab, in which yellow refers to charge density contour with the isovalue of 0.0001 e/bohr³. Cyan represents Co and red represents O atoms. Electroreduction of CO_2 to formate by Co_3O_4 with different thicknesses: (**e**) LSV curves in the CO_2-saturated (solid line) and N_2-saturated (dashed line) 0.1 M $KHCO_3$ aqueous solutions. (**f**) Faradaic efficiencies for formate at each applied potential for 4 h. (**g**) Charging current density differences plotted against scan rates. (**h**) ECSA—corrected current densities vs. applied potentials. Reprinted from [93], Copyright (2016), with permission from Wiley.
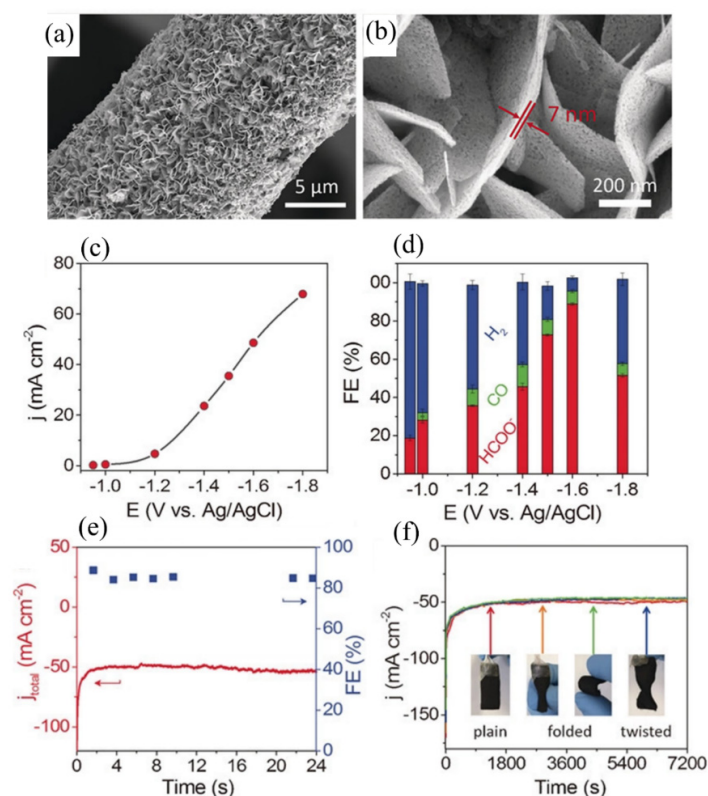
Figure 8. (**a**,**b**) The scanning electron microscope (SEM) images of porous SnO_2 nanosheets on carbon cloth (SnO_2/CC). (**c**) Current density of the SnO_2/CC electrode in CO_2-saturated 0.5 M $NaHCO_3$ solution at different applied potentials. (**d**) Corresponding FE for formate, CO and H_2. (**e**) i–t curve and FE for formate of SnO_2/CC electrode in CO_2-saturated 0.5 M $NaHCO_3$ solution at an applied potential of -1.6 V for 24 h. (**f**) i–t curves of the SnO_2/CC electrode at -1.6 V after folding or twisting 10 times. Reprinted from [95], Copyright (2017), with permission from Wiley.
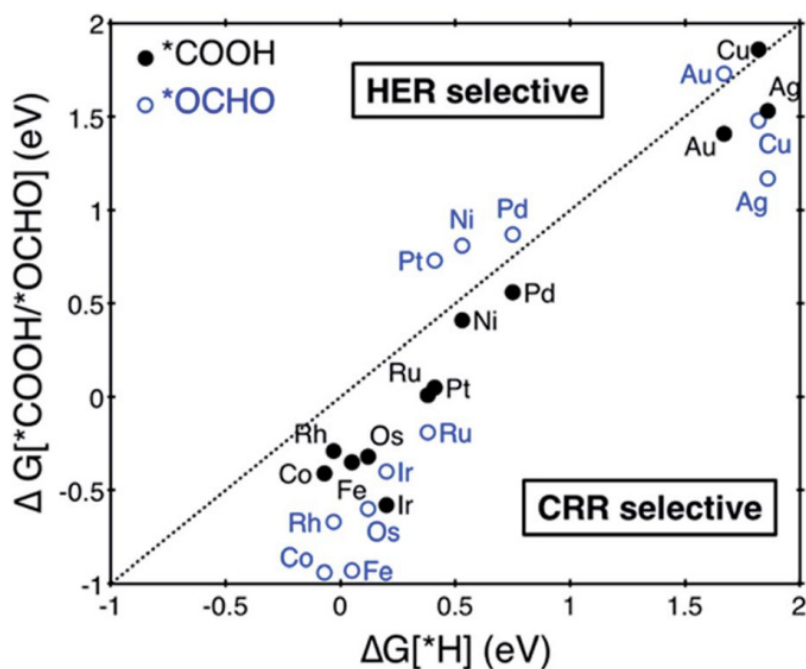

Figure 9. Free energy change in the first protonation step in ECR and HER on different SACs. Catalysts below the dotted parity line are ECR selective. Reprinted from [152], Copyright (2017), with permission from Royal Society of Chemistry.

Constructing a 3*d* transition metal-Nitrogen atom ($M–N_x$) system based on 2D materials for ECR is prevailing. Huan et al. investigated activity and selectivity of N-doped $Fe–N_4$ and Fe nanoparticles' moieties. They reported that samples with $Fe–N_4$ active sites had an FE of 80% for CO generation, but Fe nanoparticles could mostly only produce H_2 [97]. Zhang et al. synthesized Fe single atoms anchored on N-doped graphene and revealed that $Fe–N_4$ with an Fe^{2+} oxidation state was the active site for ECR [98]. They also recognized that N dopants on the graphene substrate can be beneficial for ECR. However, there are some debates on the active sites and the corresponding ECR mechanisms on Fe SACs. For instance, Zhang et al. synthesized single Fe atoms anchored on N–doped graphene by prolonged thermal pyrolysis [99]. The SAC exhibited a high FE of about 97.0% for CO production under a low overpotential of 0.35 V. The excellent performance resulted from the presence of highly efficient dispersed $Fe–N_5$ active sites. Theoretical calculations disclosed that a fifth N atom coordinated to Fe^{3+} to form $Fe–N_5$ moieties, where the additional axial pyrrolic N ligand further depleted the electron density of Fe 3*d* orbitals and reduced the π back-donation of Fe–CO bonding, which resulted in rapid CO desorption and high selectivity for CO formation.

Zhang et al. reported on single Fe atoms confined in carbon foams forming $Fe–N_4$ active sites [100]. However, they also detected an Fe^{3+} state in their samples because Fe^{2+} can be oxidized to Fe^{3+} when the samples are exposed to air, but the difference was not distinguishable in ECR. Gu et al. investigated single Fe atoms loaded on N-doped carbon with an overpotential as low as 0.08 V for CO production [101]. They confirmed the persistent presence of Fe^{3+} in the whole ECR process by in situ X-ray absorption near edge structure (XANES) measurements. Further studies indicated that $Fe^{3+}–N–C$ showed better performance for CO formation than that of $Fe^{2+}–N–C$ because of weaker CO absorption on the Fe^{3+} sites. Yang et al. prepared a N-anchored Zn single-atom catalyst on carbon [102]. From HAADF-STEM characterization, it can be clearly seen that an individual single Zn atom was supported on carbon (Figure 10a), and extended X-ray absorption fine-structure (EXAFS) spectra demonstrated the existence of a $Zn-N_4$ moiety (Figure 10b). The catalyst could reduce CO_2 to CO with high selectivity and a high FE of about 95% under the potential of -0.43 V (Figure 10c). It also exhibited remarkable durability over 75 h without any FE_{CO} decay (Figure 10d). Further experimental work and DFT calculations suggested that the remarkable activity can be attributed to the existence of $Zn–N_4$, which was the main active site for ECR and had a low free energy barrier for the rate-limiting step of *COOH formation. Zhao et al. synthesized a single Ni atom loaded on graphene oxide. The catalyst showed an FE for CO production of 96.5% at a potential of -0.63V, with a TOF of 325.9/h [103].

Yang et al. prepared a single Ni atom catalyst supported on N-doped graphene. The TOF reached 14,800/h, and the FE of CO was 97% at a potential of -0.61 V [104]. The catalyst also displayed great stability with very stable electrocatalytic activity for 100 h. Liu et al. constructed a model SAC with precise structure using two-steps by linking Ni–TAPc to CNTs and by C–C coupling [105]. This model Ni SAC exhibited excellent activity, selectivity and durability in CO_2 conversion to CO. Experimental study suggested that Ni^+ in Ni–TAPc is highly active for CO_2 activation and is the catalytically active site. In addition, the study suggested that $*CO_2^- + H^+$ to *COOH is the rate-determining step. Gong et al. prepared a series of single-atom Ni catalysts ($Ni–SA–N_x–C$) with different N coordination numbers by controlling the pyrolysis temperature [106]. Figure 11a,b clearly indicates the existence of isolated Ni atoms from TEM characterizations. The homogeneous distribution of Ni, N and C is demonstrated by energy dispersive spectroscopy (EDS) mapping (Figure 11c). It was found that the sample with $Ni–N_2$ moiety showed a higher current density than $Ni–N_3–C$ and $Ni–N_4$ in CO_2-saturated 0.5 M $KHCO_3$, indicating the best activity of $NiSA–N_2–C$ among all three SACs (Figure 11d). In addition, it exhibited a maximum FE_{CO} of 98% at -0.8 V, which is also the highest (Figure 11e). The TOF for CO production on $NiSA–N_2–C$ reached 3467 h^{-1} at the potential of -1.0 V, which is much higher than those of $NiSA–N_4–C$ and $NiSA-N_3-C$ (Figure 11f), elucidating that the coordi-

nation environment plays a crucial role in ECR performance. The current density and FE for CO generation were almost unchanged on the NiSA–N$_2$–C catalyst after electrolyzation for 10 h at the potential of −0.8 V vs. RHE (Figure 11g), demonstrating excellent stability. DFT calculations suggested that the reaction path is proton-coupled electron transfer (Figure 11h). The low N coordinated single-atom Ni sites in NiSA–N$_2$–C are beneficial for the formation of *COOH intermediate, thereby enhancing ECR activity (Figure 11i).
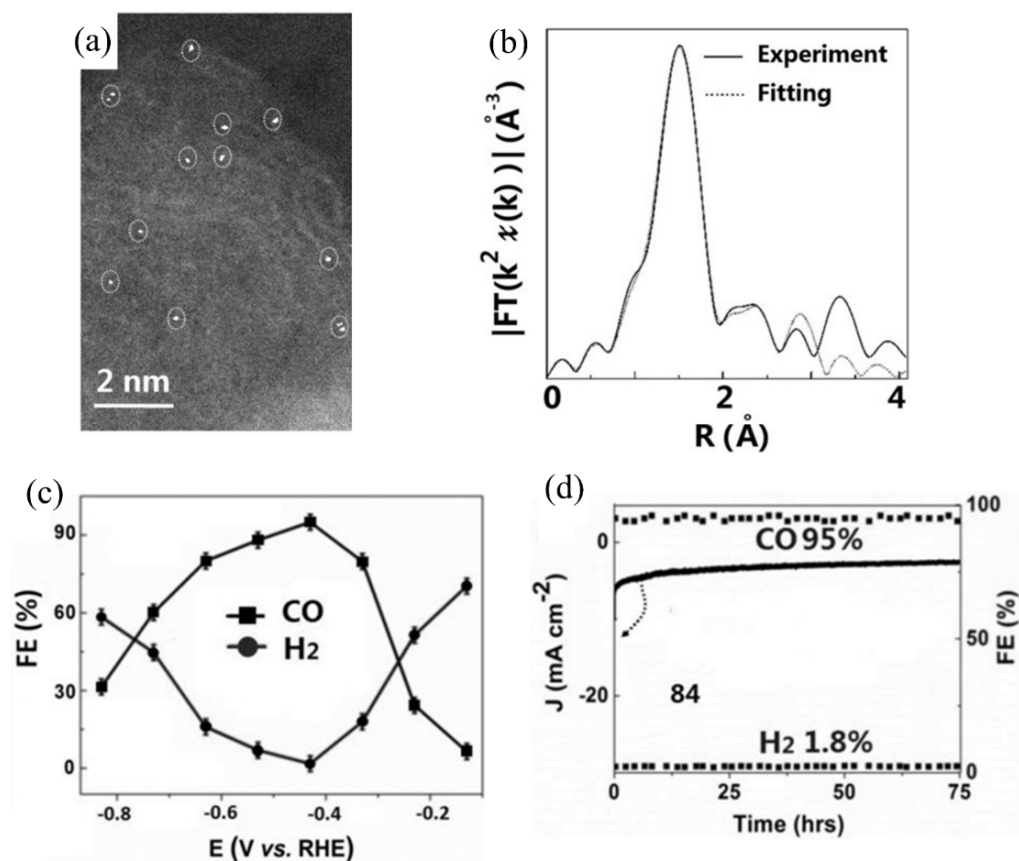

Figure 10. (**a**) Typical high-angle annular dark-field scanning transmission electron microscope (HAADF-STEM) image of the optimal ZnN$_x$/C catalyst. The circles indicate the individual Zn atoms. (**b**) A typical fitting curve of the EXAFS signal in R-space for the adsorbed ZnN$_x$/C catalyst. (**c**) FEs of CO and H$_2$ at various applied potentials on ZnN$_x$/C catalyst. (**d**) Long-term stability of ZnN$_x$/C at a potential load of −0.43 V and the corresponding FEs of CO and H$_2$. Reprinted from [102] Copyright (2018), with permission from Wiley.

Han et al. designed a free-standing ultrathin 2D SAC by self-assembly of a Co–porphyrin complex, which showed a CO production FE of 96% under an overpotential of 0.5 V [107]. They indicated that the improvement of activity was attributed to nitrogen coordination from the bottom layer, which increased the d_z energy level of the Co atoms. Jiang et al. investigated a series of SACs supported on graphene nanosheets with different defect structures [153]. Ni SAC exhibited a CO formation FE of 95% under an overpotential of 0.55 V and excellent stability. Experimental study and theoretical calculations suggested that Ni sites with slightly larger vacancies benefit CO$_2$ conversion to CO by decreasing CO desorption barrier. Recently, Zheng et al. investigated ECR performance of Cu SACs on a N-doped graphene matrix with a highly exposed and coordinatively unsaturated Cu–N$_2$ center, as shown in Figure 12a [108]. Experimental work showed an onset potential of −0.33 V and FE for CO production of about 81% under a low potential of −0.50 V vs. RHE, obviously higher than the sample with Cu–N$_4$ moiety (Figure 12b). DFT calculations manifested that Cu–N$_2$ centers can facilitate CO$_2$ activation and accelerate electron transfer from Cu–N$_2$ sites to *CO$_2$, which can greatly improve *COOH generation and the overall

ECR activity. Jiao et al. investigated a single Cu atom catalyst anchored on g-C_3N_4 as an electrocatalyst for CO_2 conversion to various hydrocarbons [154]. A slightly negative shift of photon energy demonstrated that N accepts extra charges from the Cu atom (Figure 12c). The authors reckoned that the *d*-orbital of Cu can be efficiently elevated by coordination with the g–C_3N_4 framework, enhancing the adsorption of carbonaceous intermediates. Therefore, Cu–g–C_3N_4 had better ECR activity with lower onset potential and exhibited a higher C_2 product rate than conventional Cu supported on nitrogen-doped graphene (Figure 12d).
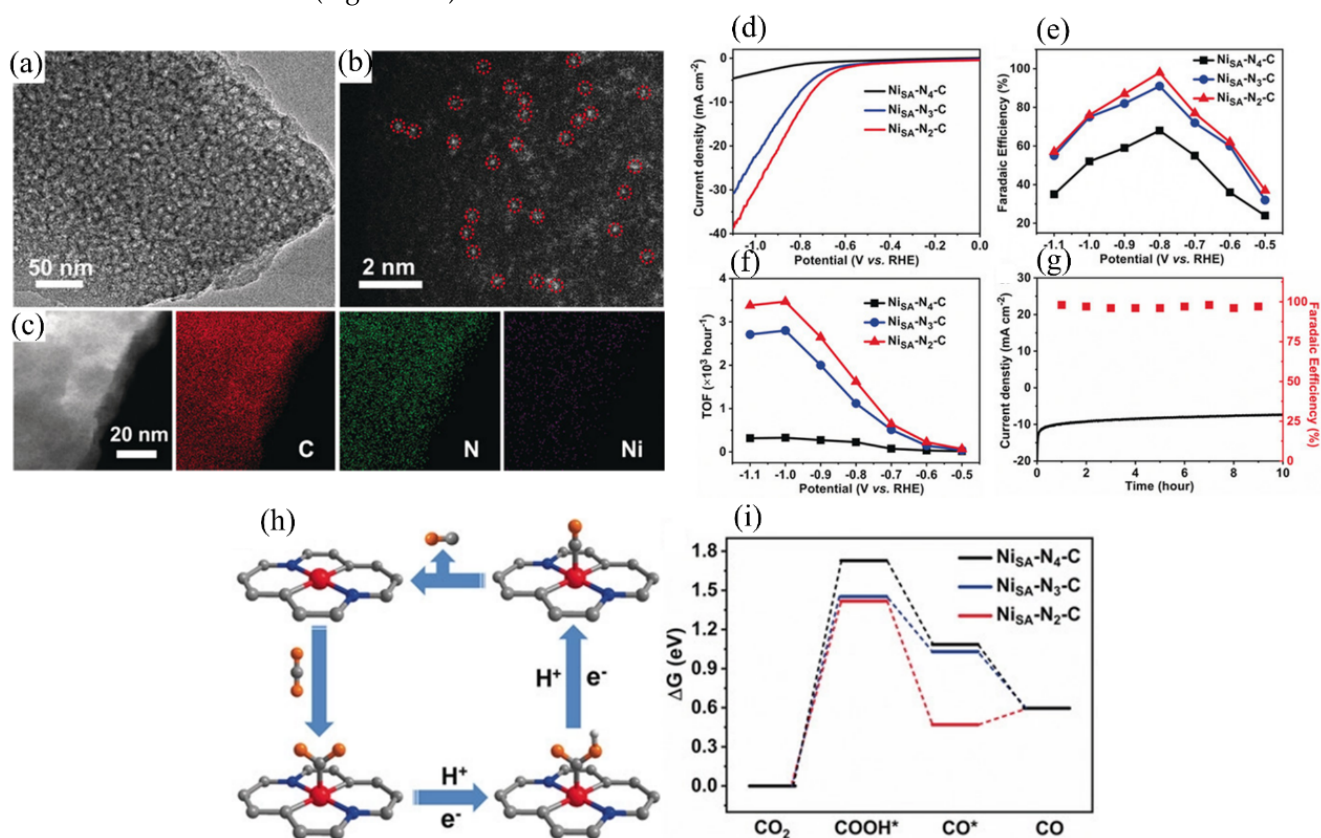

Figure 11. (**a**) Transmission electron microscope (TEM) and (**b**) HAADF-STEM images of NiSA–N_2–C. (**c**) EDS mapping of Ni, N and C elements in NiSA–N_2–C. (**d**) LSV curves in CO_2-saturated 0.5 M $KHCO_3$ electrolyte. (**e**) FEs of CO at different applied potentials. (**f**) The corresponding TOFs of CO production over NiSA–N_x–C. (**g**) Stability of NiSA–N_2–C at −0.8 V during 10 h. (**h**) Proposed reaction paths for ECR with NiSA–N_2–C as an example. (**i**) Free-energy diagram of CO_2 reduction to CO over NiSA–N_x–C catalysts. Reprinted from [106], Copyright (2020), with permission from Wiley.

Single-metal-atom-loaded 2D materials are a class of very promising catalysts for ECR due to their high atom utilization and catalytic activity. Their activity is determined by the type of metal atom and the electronic structures of the metal atom. Furthermore, the coordination number of metal atoms can be tuned by the 2D materials' support, which can further optimize the activity and selectivity of the SACs.
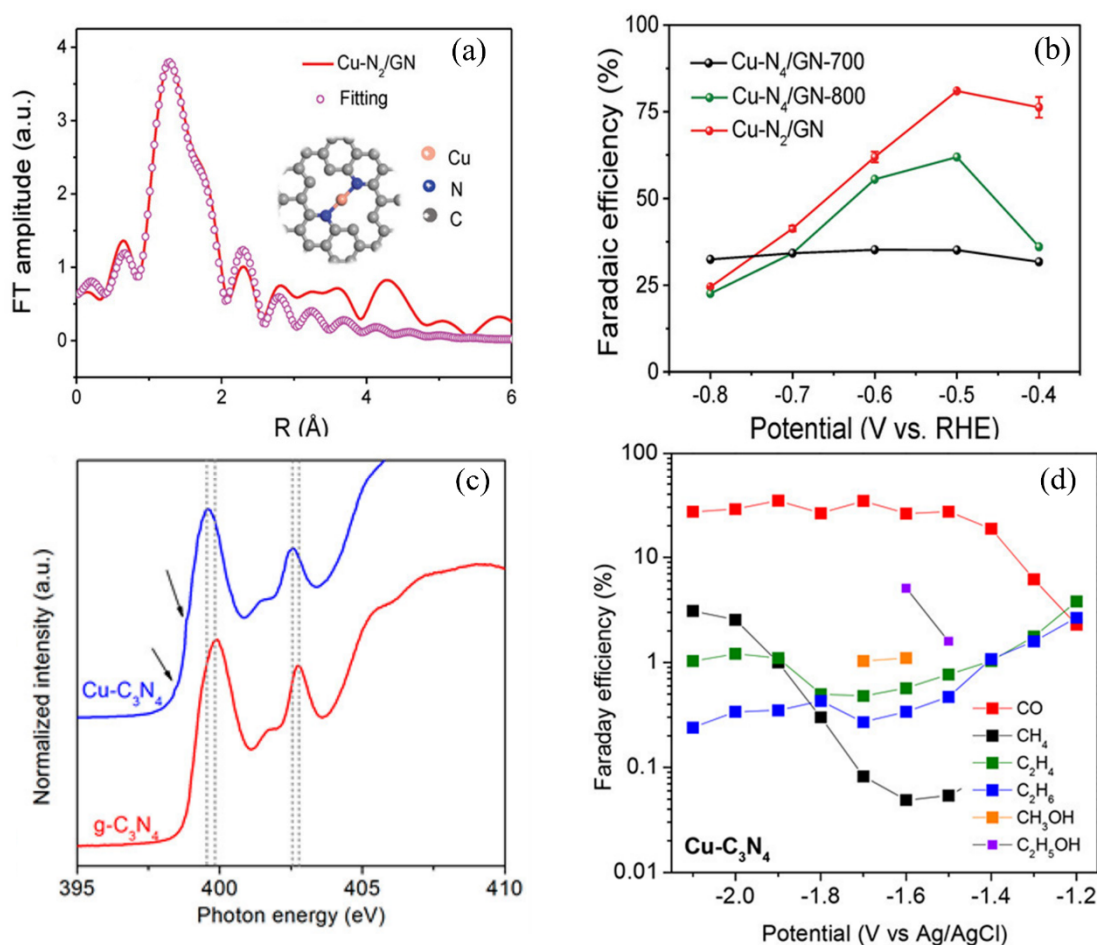
Figure 12. (**a**) Fourier transformed (FT)-EXAFS fitting results of Cu–N_2/GN. (**b**) CO FE of Cu–N_4/GN–700, Cu–N_4/GN–800 and Cu–N_2/GN. Reprinted from [108], Copyright 2020, with permission from Wiley. (**c**) Nitrogen K-edge NEXAFS of Cu–C_3N_4 and pure g–C_3N_4. Arrows show the weak shoulders in the N K-edge assigned to the Cu–N interaction. Dotted lines show the channels of photon energy in the two samples. (**d**) Measured Faradaic efficiencies of various products on Cu–C_3N_4. Reprinted from [154], Copyright (2017), with permission from American Chemical Society.

4. The Design of Electrolyzers

Numerous ECR studies are based on H-cells because they can be used conveniently to evaluate the activity of catalysts due to their easy operation and adaptability to different electrode materials and configurations [155,156]. A typical H-cell electrolyzer contains two chambers that are separated by an ion exchange membrane. The counter electrode is in the anodic chamber, whereas the working electrode and reference electrode are in the cathodic chamber. During the ECR process, CO_2 is first dissolved in the liquid catholyte, such as $KHCO_3$ and $NaHCO_3$, and then transferred to the surface of the working electrode where ECR occurs. However, the thick diffusion layer and low solubility of CO_2 in water limit CO_2 mass transport to the catalyst surface, impeding its practical applications [157].

Commercial ECR application requires continuous operation to realize high production efficiency. A microfluidic reactor for ECR has been designed where the electrolyte can continuously flow through the electrolyzer [158,159]. The cathode and anode are separated by a very thin channel that is filled with flowing electrolytes. CO_2 is supplied from the back of the cathodic gas diffusion electrode (GDE), and ECR occurs when CO_2 reaches the surface of catalysts. The operation parameters, such as the composition and pH of the electrolyte, can be adjusted, which promotes ECR rates. GDEs are high-surface-area and porous electrodes. A typical GDE consists of a catalytic layer, a gas diffusion layer and a gas flow field. The structure and composition of GDE layers play a vital

role in the transport of reactants and products because the transport processes influence the accumulation or depletion of intermediates on the catalysts, which determine ECR performance [160,161]. Lim et al. prepared Sn electrocatalysts with dense tips (SnDT) GDE, showing formate productivity of 65 mg h^{-1}. It was stable for 72 h without changes in FE or current density [162]. A 2D nanosheet Cu-loaded GDE achieved the highest partial current density of 131 mA cm^{-2} for acetate production [163]. Although high current density was realized, the microfluidic reactor still suffered product crossover, where the reduction of oxygen diffused to the cathode and the reoxidation of cathodic products diffused to the anode, decreasing the overall energy efficiency and productivity.

The membrane electrode assembly (MEA) electrolyzers have been exploited to solve problems of the microfluidic reactors. The catalytic layer of cathodic GDEs is in direct contact with the polymer electrolyte membranes. MEAs can decrease ohmic losses and prevent the poison of cathode catalysts by impurities through removing catholyte between the membrane and GDE. As a result, MEAs can exhibit excellent stability and high energy efficiency [164]. Gas and liquid products flow out of the cathode flow plate with little diffusion into catholyte through the membrane, resulting in high concentration liquid product. Cobalt phthalocyanine (Co-Pc) has been widely studied for ECR to CO in both immobilized and homogeneous forms and was also used in an MEA system with FE of CO >90% over 8 h at 50 mA cm^{-2} [165]. Gabardo et al. designed an MEA electrolyzer that achieved an FE of ~80% for higher carbon products such as ethylene, ethanol, acetate and 1-propanol with current densities >100 mA cm^{-2} for 100 h [164].

5. Conclusions and Perspectives

Electrochemical reduction reactions are a promising strategy to convert CO_2 into valuable fuels and chemical products, which can offer potential technological solutions for energy problems and greenhouse effects. An effective electrocatalyst is the key to the potential deployment of commercial ECR processes. In this contribution, we review a series of 2D materials, including metal, graphene-based materials, TMDs, MOFs materials, metal oxide nanosheets and 2D materials incorporated with single atoms as ECR catalysts. Compared to the conventional metal-based electrocatalysts, 2D materials show unique physicochemical properties and electronic structures benefiting ECR activity.

Nevertheless, there are still challenges in the design and synthesis of 2D electrocatalysts for ECR. To date, most ECR catalysts can only produce C_1 products, especially CO, while producing more valuable products, such as C_2 and C_3 products, is desired. In general, the intrinsic activity can be modified in various ways such as doping, constructing special structures and morphologies, etc. Meanwhile, the choices of different classes of 2D materials are important for producing specific products. Strategies, such as constructing composite electrocatalyst materials and surface engineering of electrocatalysts, could be employed. Composite electrocatalyst materials could have different properties and catalytic performance in comparison with individual components due to synergistic effects. They could possess excellent properties for ECR such as better conductivity, high specific surface area, more active sites, better transport property and high durability. Another strategy is surface engineering of electrocatalysts by synthesizing nanotubes, nanosheets, nanospheres, isolated single atoms and defects. These properties are beneficial for effective contact for electrolyte ions and adsorption and desorption of intermediates. It is worth noting that single metal atoms anchored on the surface of 2D materials as SACs have rather high efficiency in ECR. However, the synthesis of SAC loaded on 2D materials is still a challenge, and key aspects, including suitable mononuclear metal complex precursors and stabilization of single metal atoms on the 2D materials, should be considered. Future research opportunities could be to develop new 2D materials such as MXenes and COFs.

Combining theoretical calculation and experimental work is necessary to obtain a fundamental understanding on the design and synthesis of 2D electrocatalysts. Although theoretical calculations are conducted with simplified models under idealized conditions, they could always be beneficial for revealing the reaction mechanism and providing guid-

ance for design principles. For instance, breaking the scaling relationships between adsorption energies of different intermediates is of great significance to improve the activity of catalysts, which can be revealed from theoretical calculations. Similarly, to mitigate catalyst deactivation in ECR, it is necessary to understand the deactivation mechanisms. Theoretical models could be constructed to predict the intermediates which affect the stability of electrocatalysts. Finally, rapid development of characterization techniques, especially in situ spectroscopy, can greatly promote the development of catalysts of ECR. In situ spectroscopy can investigate catalytic reactions under reaction conditions and provide insights into the true active sites and reaction mechanisms. Through in situ techniques, such as infrared spectroscopy, Raman spectroscopy, X-ray absorption spectroscopy, X-ray photoelectron spectroscopy, mass spectrometry, etc., crucial issues in ECR, including identifying reaction intermediates, active sites and reaction pathways, can be resolved.

H-type cells are widely used in ECR. The current density of an H-type cell is limited to tens of milliamps, which is far from industrial application due to limited CO_2 solubility and energy loss. The design of microfluidic flow cells has made great progress recently. For example, the GDE and MEA electrolyzers can effectively tune reaction conditions and local environments in ECR. GDEs utilize a porous catalyst layer along with diffusion media, which can promote reactant transport. Thus, high current density can be realized, and transport losses can be effectively avoided. In the flow cell, higher carbon products are favored at high pH values, which can be hardly realized in an H-type cell. Flow cells and MEA make the separation of products convenient. These advantages could effectively accelerate the large-scale application of ECR at the industrial level.

It has been demonstrated that 2D nanomaterials possess great potential for ECR. Nevertheless, most of the 2D materials discussed in this review are still far from practical application. It is still demanding to synthesize 2D electrocatalysts with excellent performance at a large scale. Therefore, it is important to narrow the gap between laboratory- and commercial-scale production. Currently, some techniques, such as strip and salt–temperature, have been applied in the large-scale synthesis of 2D materials, but scalable routes to prepare ultrathin nanosheets remain to be developed.

Author Contributions: Conceptualization, S.L., F.L. and Z.Y.; investigation, S.L. and Z.Y.; writing—original draft preparation, S.L. and Z.Y.; writing—review and editing, S.L., F.L. and Z.Y.; funding acquisition, Z.Y.; supervision, F.L. and Z.Y. All authors have read and agreed to the published version of the manuscript.

Data Availability Statement: Not applicable.

Conflicts of Interest: The authors declare no conflict of interest.

References

1. Caldeira, K.; Wickett, M.E. Anthropogenic carbon and ocean pH. *Nature* **2003**, *425*, 365. [CrossRef] [PubMed]
2. Fu, Y.; Sun, D.; Chen, Y.; Huang, R.; Ding, Z.; Fu, X.; Li, Z. An amine-functionalized titanium metal-organic framework photocatalyst with visible-light-induced activity for CO_2 reduction. *Angew. Chem. Int. Ed.* **2012**, *51*, 3364–3367. [CrossRef]
3. Li, J.R.; Ma, Y.; McCarthy, M.C.; Sculley, J.; Yu, J.; Jeong, H.K.; Balbuena, P.B.; Zhou, H.C. Carbon dioxide capture-related gas adsorption and separation in metal-organic frameworks. *Coord. Chem. Rev.* **2011**, *255*, 1791–1823. [CrossRef]
4. Li, X.; Yu, J.; Jaroniec, M.; Chen, X. Cocatalysts for Selective Photoreduction of CO_2 into Solar Fuels. *Chem. Rev.* **2019**, *119*, 3962–4179. [CrossRef] [PubMed]
5. Rubin, E.S.; Davison, J.E.; Herzog, H.J. The cost of CO_2 capture and storage. *Int. J. Greenh. Gas Control* **2015**, *40*, 378–400. [CrossRef]
6. Keith, D.W.; Holmes, G.; St Angelo, D.; Heidel, K. A Process for Capturing CO_2 from the Atmosphere. *Joule* **2018**, *2*, 1573–1594. [CrossRef]
7. Drage, T.C.; Snape, C.E.; Stevens, L.A.; Wood, J.; Wang, J.; Cooper, A.I.; Dawson, R.; Guo, X.; Satterley, C.; Irons, R. Materials challenges for the development of solid sorbents for post-combustion carbon capture. *J. Mater. Chem.* **2012**, *22*, 2815–2823. [CrossRef]
8. Orr, J.F.M. CO_2 capture and storage: Are we ready? *Energy Environ. Sci.* **2009**, *2*, 449–458. [CrossRef]
9. Maginn, E.J. What to Do with CO_2. *J. Phys. Chem. Lett.* **2010**, *1*, 3478–3479. [CrossRef]

10. Ramdin, M.; de Loos, T.W.; Vlugt, T.J.H. State-of-the-Art of CO$_2$ Capture with Ionic Liquids. *Ind. Eng. Chem. Res.* **2012**, *51*, 8149–8177. [CrossRef]

11. Wang, J.Y.; Huang, L.; Yang, R.Y.; Wu, J.W.; Gao, Y.S.; Wang, Q.; O'Hare, D.; Zhong, Z.Y. Recent advances in solid sorbents for CO$_2$ capture and new development trends. *Energy Environ. Sci.* **2014**, *7*, 3478–3518. [CrossRef]

12. Yu, C.H.; Huang, C.H.; Tan, C.S. A Review of CO$_2$ Capture by Absorption and Adsorption. *Aerosol Air Qual. Res.* **2012**, *12*, 745–769. [CrossRef]

13. Inoue, T.; Fujishima, A.; Konishi, S.; Honda, K. Photoelectrocatalytic reduction of carbon dioxide in aqueous suspensions of semiconductor powders. *Nature* **1979**, *277*, 637–638. [CrossRef]

14. Halmann, M. Photoelectrochemical reduction of aqueous carbon dioxide on p-type gallium phosphide in liquid junction solar cells. *Nature* **1978**, *275*, 115–116. [CrossRef]

15. Li, W. Electrocatalytic Reduction of CO$_2$ to Small Organic Molecule Fuels on Metal Catalysts. In *Advances in CO$_2$ Conversion and Utilization*; ACS Symposium Series; ACS Publisher: Washington, DC, USA, 2010; Volume 1056, pp. 55–76. [CrossRef]

16. Kortlever, R.; Peters, I.; Koper, S.; Koper, M.T.M. Electrochemical CO$_2$ Reduction to Formic Acid at Low Overpotential and with High Faradaic Efficiency on Carbon-Supported Bimetallic Pd–Pt Nanoparticles. *ACS Catal.* **2015**, *5*, 3916–3923. [CrossRef]

17. Zafar, Q.; Mattisson, T.; Gevert, B. Integrated Hydrogen and Power Production with CO$_2$ Capture Using Chemical-Looping ReformingsRedox Reactivity of Particles of CuO, Mn$_2$O$_3$, NiO, and Fe$_2$O$_3$ Using SiO$_2$ as a Support. *Ind. Eng. Chem. Res.* **2005**, *44*, 3485–3496. [CrossRef]

18. Chen, X.; Wang, J.; Huang, C.; Zhang, S.; Zhang, H.; Li, Z.; Zou, Z. Barium zirconate: A new photocatalyst for converting CO$_2$ into hydrocarbons under UV irradiation. *Catal. Sci. Technol.* **2015**, *5*, 1758–1763. [CrossRef]

19. Ding, J.; Bu, Y.; Ou, M.; Yu, Y.; Zhong, Q.; Fan, M. Facile decoration of carbon fibers with Ag nanoparticles for adsorption and photocatalytic reduction of CO$_2$. *Appl. Catal. B Environ.* **2017**, *202*, 314–325. [CrossRef]

20. Wang, W.; Wang, S.; Ma, X.; Gong, J. Recent advances in catalytic hydrogenation of carbon dioxide. *Chem. Soc. Rev.* **2011**, *40*, 3703–3727. [CrossRef]

21. Shi, J.F.; Jiang, Y.J.; Jiang, Z.Y.; Wang, X.Y.; Wang, X.L.; Zhang, S.H.; Han, P.P.; Yang, C. Enzymatic conversion of carbon dioxide. *Chem. Soc. Rev.* **2015**, *44*, 5981–6000. [CrossRef]

22. Gong, Q.; Ding, P.; Xu, M.; Zhu, X.; Wang, M.; Deng, J.; Ma, Q.; Han, N.; Zhu, Y.; Lu, J.; et al. Structural defects on converted bismuth oxide nanotubes enable highly active electrocatalysis of carbon dioxide reduction. *Nat. Commun.* **2019**, *10*, 2807. [CrossRef] [PubMed]

23. Li, T.T.; Shan, B.; Xu, W.; Meyer, T.J. Electrocatalytic CO$_2$ Reduction with a Ruthenium Catalyst in Solution and on Nanocrystalline TiO$_2$. *ChemSusChem* **2019**, *12*, 2402–2408. [CrossRef] [PubMed]

24. Grodkowski, J.; Neta, P. Copper-Catalyzed Radiolytic Reduction of CO$_2$ to CO in Aqueous Solutions. *J. Phys. Chem. B* **2001**, *105*, 4967–4972. [CrossRef]

25. Agarwal, A.S.; Zhai, Y.; Hill, D.; Sridhar, N. The electrochemical reduction of carbon dioxide to formate/formic acid: Engineering and economic feasibility. *ChemSusChem* **2011**, *4*, 1301–1310. [CrossRef]

26. Pritchard, J.; Filonenko, G.A.; van Putten, R.; Hensen, E.J.; Pidko, E.A. Heterogeneous and homogeneous catalysis for the hydrogenation of carboxylic acid derivatives: History, advances and future directions. *Chem. Soc. Rev.* **2015**, *44*, 3808–3833. [CrossRef]

27. Zhu, Q.; Sun, X.; Yang, D.; Ma, J.; Kang, X.; Zheng, L.; Zhang, J.; Wu, Z.; Han, B. Carbon dioxide electroreduction to C$_2$ products over copper-cuprous oxide derived from electrosynthesized copper complex. *Nat. Commun.* **2019**, *10*, 3851. [CrossRef]

28. Gao, S.; Lin, Y.; Jiao, X.; Sun, Y.; Luo, Q.; Zhang, W.; Li, D.; Yang, J.; Xie, Y. Partially oxidized atomic cobalt layers for carbon dioxide electroreduction to liquid fuel. *Nature* **2016**, *529*, 68–71. [CrossRef]

29. Kaneco, S.; Katsumata, H.; Suzuki, T.; Ohta, K. Electrochemical reduction of carbon dioxide to ethylene at a copper electrode in methanol using potassium hydroxide and rubidium hydroxide supporting electrolytes. *Electrochim. Acta* **2006**, *51*, 3316–3321. [CrossRef]

30. Lu, Q.; Rosen, J.; Zhou, Y.; Hutchings, G.S.; Kimmel, Y.C.; Chen, J.G.; Jiao, F. A selective and efficient electrocatalyst for carbon dioxide reduction. *Nat. Commun.* **2014**, *5*, 3242. [CrossRef]

31. Durand, W.J.; Peterson, A.A.; Studt, F.; Abild-Pedersen, F.; Nørskov, J.K. Structure effects on the energetics of the electrochemical reduction of CO$_2$ by copper surfaces. *Surf. Sci.* **2011**, *605*, 1354–1359. [CrossRef]

32. Siahrostami, S.; Jiang, K.; Karamad, M.; Chan, K.; Wang, H.; Nørskov, J. Theoretical Investigations into Defected Graphene for Electrochemical Reduction of CO$_2$. *ACS Sustain. Chem. Eng.* **2017**, *5*, 11080–11085. [CrossRef]

33. Chen, Y.; Li, C.W.; Kanan, M.W. Aqueous CO$_2$ reduction at very low overpotential on oxide-derived Au nanoparticles. *J. Am. Chem. Soc.* **2012**, *134*, 19969–19972. [CrossRef]

34. Sui, S.; Wang, X.; Zhou, X.; Su, Y.; Riffat, S.; Liu, C.j. A comprehensive review of Pt electrocatalysts for the oxygen reduction reaction: Nanostructure, activity, mechanism and carbon support in PEM fuel cells. *J. Mater. Chem. A* **2017**, *5*, 1808–1825. [CrossRef]

35. Gattrell, M.; Gupta, N.; Co, A. A review of the aqueous electrochemical reduction of CO$_2$ to hydrocarbons at copper. *J. Electroanal. Chem.* **2006**, *594*, 1–19. [CrossRef]

36. Chernikov, A.; van der Zande, A.M.; Hill, H.M.; Rigosi, A.F.; Velauthapillai, A.; Hone, J.; Heinz, T.F. Electrical Tuning of Exciton Binding Energies in Monolayer WS$_2$. *Phys. Rev. Lett.* **2015**, *115*, 126802. [CrossRef] [PubMed]

37. Wang, H.; Yuan, H.; Sae Hong, S.; Li, Y.; Cui, Y. Physical and chemical tuning of two-dimensional transition metal dichalcogenides. *Chem. Soc. Rev.* **2015**, *44*, 2664–2680. [CrossRef]

38. Wang, H.; Chen, Y.; Hou, X.; Ma, C.; Tan, T. Nitrogen-doped graphenes as efficient electrocatalysts for the selective reduction of carbon dioxide to formate in aqueous solution. *Green Chem.* **2016**, *18*, 3250–3256. [CrossRef]

39. Ao, C.; Feng, B.; Qian, S.; Wang, L.; Zhao, W.; Zhai, Y.; Zhang, L. Theoretical study of transition metals supported on g-C$_3$N$_4$ as electrochemical catalysts for CO$_2$ reduction to CH$_3$OH and CH$_4$. *J. CO2 Util.* **2020**, *36*, 116–123. [CrossRef]

40. Zhi, X.; Jiao, Y.; Zheng, Y.; Qiao, S.Z. Impact of Interfacial Electron Transfer on Electrochemical CO$_2$ Reduction on Graphitic Carbon Nitride/Doped Graphene. *Small* **2019**, *15*, e1804224. [CrossRef]

41. Kong, D.; Cha, J.J.; Wang, H.; Lee, H.R.; Cui, Y. First-row transition metal dichalcogenide catalysts for hydrogen evolution reaction. *Energy Environ. Sci.* **2013**, *6*, 3553–3558. [CrossRef]

42. Chhowalla, M.; Shin, H.S.; Eda, G.; Li, L.J.; Loh, K.P.; Zhang, H. The chemistry of two-dimensional layered transition metal dichalcogenide nanosheets. *Nat. Chem.* **2013**, *5*, 263–275. [CrossRef] [PubMed]

43. Wang, Q.; Zhang, Y.; Lin, H.; Zhu, J. Recent Advances in Metal-Organic Frameworks for Photo-/Electrocatalytic CO$_2$ Reduction. *Chem. Eur. J.* **2019**, *25*, 14026–14035. [CrossRef] [PubMed]

44. Olabi, A.G.; Abdelkareem, M.A.; Wilberforce, T.; Sayed, E.T. Application of Graphene in Energy Storage Device—A Review. *Renew. Sustain. Energy Rev.* **2021**, *135*, 110026. [CrossRef]

45. Yu, Y.; Wang, T.; Chen, X.; Zhang, L.; Wang, Y.; Niu, Y.; Yu, J.; Ma, H.; Li, X.; Liu, F.; et al. Demonstration of epitaxial growth of strain-relaxed GaN films on graphene/SiC substrates for long wavelength light-emitting diodes. *Light Sci. Appl.* **2021**, *117*. [CrossRef] [PubMed]

46. Ishikawa, R.; Yamazaki, S.; Watanabe, S.; Tsuboi, N. Layer dependency of graphene layers in perovskite/graphene solar cells. *Carbon* **2021**, *172*, 597–601. [CrossRef]

47. Nag, A.; Mitra, A.; Mukhopadhyay, S.C. Graphene and its sensor-based applications: A review. *Sens. Actuators A Phys.* **2018**, *270*, 177–194. [CrossRef]

48. Nemiwal, M.; Zhang, T.C.; Kumar, D. Graphene-based electrocatalysts: Hydrogen evolution reactions and overall water splitting. *Int. J. Hydrogen Energy* **2021**, *46*, 21401–21418. [CrossRef]

49. Wang, G.; Chen, J.; Ding, Y.; Cai, P.; Yi, L.; Li, Y.; Tu, C.; Hou, Y.; Wen, Z.; Dai, L. Electrocatalysis for CO$_2$ conversion: From fundamentals to value-added products. *Chem. Soc. Rev.* **2021**, *50*, 4993–5061. [CrossRef]

50. Nitopi, S.; Bertheussen, E.; Scott, S.B.; Liu, X.; Engstfeld, A.K.; Horch, S.; Seger, B.; Stephens, I.E.L.; Chan, K.; Hahn, C.; et al. Progress and Perspectives of Electrochemical CO2 Reduction on Copper in Aqueous Electrolyte. *Chem. Rev.* **2019**, *119*, 7610–7672. [CrossRef]

51. Jin, L.; Seifitokaldani, A. In Situ Spectroscopic Methods for Electrocatalytic CO$_2$ Reduction. *Catalysts* **2020**, *10*, 481. [CrossRef]

52. Zhu, Y.; Yang, X.; Peng, C.; Priest, C.; Mei, Y.; Wu, G. Carbon-Supported Single Metal Site Catalysts for Electrochemical CO$_2$ Reduction to CO and Beyond. *Small* **2021**, *17*, e2005148. [CrossRef] [PubMed]

53. Zhu, X.; Li, Y. Review of two-dimensional materials for electrochemical CO$_2$ reduction from a theoretical perspective. *Wiley Interdiscip. Rev. Comput. Mol. Sci.* **2019**, *9*, e1416. [CrossRef]

54. Zhang, W.; Ma, D.; Pérez-Ramírez, J.; Chen, Z. Recent Progress in Materials Materials Exploration for Thermocatalytic, Photocatalytic, and Integrated Photothermocatalytic CO$_2$ to Fuel Conversion. *Adv. Sustain. Syst.* **2021**, *3*, 2100169. [CrossRef]

55. Zhang, W.; Jin, Z.; Chen, Z. Rational-Designed Principles for Electrochemical and Photoelectrochemical Upgrading of CO$_2$ to Value-Added Chemicals. *Adv. Sci.* **2022**, e2105204. [CrossRef]

56. Li, Q.; Wang, Y.C.; Zeng, J.; Zhao, X.; Chen, C.; Wu, Q.M.; Chen, L.M.; Chen, Z.Y.; Lei, Y.P. Bimetallic chalcogenides for electrocatalytic CO$_2$ reduction. *Rare Met.* **2021**, *40*, 3442–3453. [CrossRef]

57. Wang, J.J.; Li, X.P.; Cui, B.F.; Zhang, Z.; Hu, X.F.; Ding, J.; Deng, Y.D.; Han, X.P.; Hu, W.B. A review of non-noble metal-based electrocatalysts for CO$_2$ electroreduction. *Rare Met.* **2021**, *40*, 3019–3037. [CrossRef]

58. Sun, Z.; Ma, T.; Tao, H.; Fan, Q.; Han, B. Fundamentals and Challenges of Electrochemical CO$_2$ Reduction Using Two-Dimensional Materials. *Chem* **2017**, *3*, 560–587. [CrossRef]

59. Zou, X.; Liu, M.; Wu, J.; Ajayan, P.M.; Li, J.; Liu, B.; Yakobson, B.I. How Nitrogen-Doped Graphene Quantum Dots Catalyze Electroreduction of CO$_2$ to Hydrocarbons and Oxygenates. *ACS Catal.* **2017**, *7*, 6245–6250. [CrossRef]

60. García Rey, N.; Dlott, D.D. Structural Transition in an Ionic Liquid Controls CO$_2$ Electrochemical Reduction. *J. Phys. Chem. C* **2015**, *119*, 20892–20899. [CrossRef]

61. Ma, T.; Fan, Q.; Li, X.; Qiu, J.; Wu, T.; Sun, Z. Graphene-based materials for electrochemical CO$_2$ reduction. *J. CO2 Util.* **2019**, *30*, 168–182. [CrossRef]

62. Benson, E.E.; Kubiak, C.P.; Sathrum, A.J.; Smieja, J.M. Electrocatalytic and homogeneous approaches to conversion of CO$_2$ to liquid fuels. *Chem. Soc. Rev.* **2009**, *38*, 89–99. [CrossRef] [PubMed]

63. Qiao, J.; Liu, Y.; Hong, F.; Zhang, J. A review of catalysts for the electroreduction of carbon dioxide to produce low-carbon fuels. *Chem. Soc. Rev.* **2014**, *43*, 631–675. [CrossRef] [PubMed]

64. Sun, Z.; Talreja, N.; Tao, H.; Texter, J.; Muhler, M.; Strunk, J.; Chen, J. Catalysis of Carbon Dioxide Photoreduction on Nanosheets: Fundamentals and Challenges. *Angew. Chem. Int. Ed.* **2018**, *57*, 7610–7627. [CrossRef]

65. Zhang, L.; Zhao, Z.J.; Gong, J. Nanostructured Materials for Heterogeneous Electrocatalytic CO$_2$ Reduction and their Related Reaction Mechanisms. *Angew. Chem. Int. Ed.* **2017**, *56*, 11326–11353. [CrossRef] [PubMed]

66. DeCiccio, D.; Ahn, S.T.; Sen, S.; Schunk, F.; Palmore, G.T.R.; Rose-Petruck, C. Electrochemical reduction of CO_2 with clathrate hydrate electrolytes and copper foam electrodes. *Electrochem. Commun.* **2015**, *52*, 13–16. [CrossRef]

67. Appel, A.M.; Bercaw, J.E.; Bocarsly, A.B.; Dobbek, H.; DuBois, D.L.; Dupuis, M.; Ferry, J.G.; Fujita, E.; Hille, R.; Kenis, P.J.; et al. Frontiers, opportunities, and challenges in biochemical and chemical catalysis of CO_2 fixation. *Chem. Rev.* **2013**, *113*, 6621–6658. [CrossRef]

68. Zhong, M.; Tran, K.; Min, Y.; Wang, C.; Wang, Z.; Dinh, C.T.; De Luna, P.; Yu, Z.; Rasouli, A.S.; Brodersen, P.; et al. Accelerated discovery of CO_2 electrocatalysts using active machine learning. *Nature* **2020**, *581*, 178–183. [CrossRef]

69. Geioushy, R.A.; Khaled, M.M.; Alhooshani, K.; Hakeem, A.S.; Rinaldi, A. Graphene/ZnO/Cu_2O electrocatalyst for selective conversion of CO_2 into n-propanol. *Electrochim. Acta* **2017**, *245*, 456–462. [CrossRef]

70. Hori, Y. Electrochemical CO_2 Reduction on Metal Electrodes. *Mod. Aspect. Electroc.* **2008**, *42*, 89–189. [CrossRef]

71. Li, F.; Zhao, S.F.; Chen, L.; Khan, A.; MacFarlane, D.R.; Zhang, J. Polyethylenimine promoted electrocatalytic reduction of CO_2 to CO in aqueous medium by graphene-supported amorphous molybdenum sulphide. *Energy Environ. Sci.* **2016**, *9*, 216–223. [CrossRef]

72. Zhu, W.; Zhang, Y.J.; Zhang, H.; Lv, H.; Li, Q.; Michalsky, R.; Peterson, A.A.; Sun, S. Active and selective conversion of CO_2 to CO on ultrathin Au nanowires. *J. Am. Chem. Soc.* **2014**, *136*, 16132–16135. [CrossRef] [PubMed]

73. Zhu, W.; Zhang, L.; Yang, P.; Hu, C.; Luo, Z.; Chang, X.; Zhao, Z.J.; Gong, J. Low-Coordinated Edge Sites on Ultrathin Palladium Nanosheets Boost Carbon Dioxide Electroreduction Performance. *Angew. Chem. Int. Ed.* **2018**, *57*, 11544–11548. [CrossRef] [PubMed]

74. Wang, Y.; Cao, L.; Libretto, N.J.; Li, X.; Li, C.; Wan, Y.; He, C.; Lee, J.; Gregg, J.; Zong, H.; et al. Ensemble Effect in Bimetallic Electrocatalysts for CO_2 Reduction. *J. Am. Chem. Soc.* **2019**, *141*, 16635–16642. [CrossRef] [PubMed]

75. Wu, J.; Liu, M.; Sharma, P.P.; Yadav, R.M.; Ma, L.; Yang, Y.; Zou, X.; Zhou, X.D.; Vajtai, R.; Yakobson, B.I.; et al. Incorporation of Nitrogen Defects for Efficient Reduction of CO_2 via Two-Electron Pathway on Three-Dimensional Graphene Foam. *Nano Lett.* **2016**, *16*, 466–470. [CrossRef]

76. Zhang, W.; Hu, Y.; Ma, L.; Zhu, G.; Zhao, P.; Xue, X.; Chen, R.; Yang, S.; Ma, J.; Liu, J.; et al. Liquid-phase exfoliated ultrathin Bi nanosheets: Uncovering the origins of enhanced electrocatalytic CO_2 reduction on two-dimensional metal nanostructure. *Nano Energy* **2018**, *53*, 808–816. [CrossRef]

77. Pan, J.; Sun, Y.; Deng, P.; Yang, F.; Chen, S.; Zhou, Q.; Park, H.S.; Liu, H.; Yu Xia, B. Hierarchical and ultrathin copper nanosheets synthesized via galvanic replacement for selective electrocatalytic carbon dioxide conversion to carbon monoxide. *Appl. Catal. B Environ.* **2019**, *255*, 117736. [CrossRef]

78. Wang, Y.; Shen, H.; Livi, K.J.T.; Raciti, D.; Zong, H.; Gregg, J.; Onadeko, M.; Wan, Y.; Watson, A.; Wang, C. Copper Nanocubes for CO_2 Reduction in Gas Diffusion Electrodes. *Nano Lett.* **2019**, *19*, 8461–8468. [CrossRef]

79. Sreekanth, N.; Nazrulla, M.A.; Vineesh, T.V.; Sailaja, K.; Phani, K.L. Metal-free boron-doped graphene for selective electroreduction of carbon dioxide to formic acid/formate. *Chem. Commun.* **2015**, *51*, 16061. [CrossRef]

80. Liu, X.; Zhu, L.; Wang, H.; He, G.; Bian, Z. Catalysis performance comparison for electrochemical reduction of CO_2 on Pd–Cu/graphene catalyst. *RSC Adv.* **2016**, *6*, 38380–38387. [CrossRef]

81. Su, P.; Iwase, K.; Nakanishi, S.; Hashimoto, K.; Kamiya, K. Nickel-Nitrogen-Modified Graphene: An Efficient Electrocatalyst for the Reduction of Carbon Dioxide to Carbon Monoxide. *Small* **2016**, *12*, 6083–6089. [CrossRef]

82. Huang, J.; Guo, X.; Wei, Y.; Hu, Q.; Yu, X.; Wang, L. A renewable, flexible and robust single layer nitrogen-doped graphene coating Sn foil for boosting formate production from electrocatalytic CO_2 reduction. *J. CO2 Util.* **2019**, *33*, 166–170. [CrossRef]

83. Lei, F.; Liu, W.; Sun, Y.; Xu, J.; Liu, K.; Liang, L.; Yao, T.; Pan, B.; Wei, S.; Xie, Y. Metallic tin quantum sheets confined in graphene toward high-efficiency carbon dioxide electroreduction. *Nat. Commun.* **2016**, *7*, 12697. [CrossRef] [PubMed]

84. Li, F.; Chen, L.; Xue, M.; Williams, T.; Zhang, Y.; MacFarlane, D.R.; Zhang, J. Towards a better Sn: Efficient electrocatalytic reduction of CO_2 to formate by Sn/SnS_2 derived from SnS_2 nanosheets. *Nano Energy* **2017**, *31*, 270–277. [CrossRef]

85. Lu, X.; Tan, T.H.; Ng, Y.H.; Amal, R. Highly Selective and Stable Reduction of CO_2 to CO by a Graphitic Carbon Nitride/Carbon Nanotube Composite Electrocatalyst. *Eur. J. Chem.* **2016**, *22*, 11991–11996. [CrossRef]

86. Guo, S.; Zhao, S.; Wu, X.; Li, H.; Zhou, Y.; Zhu, C.; Yang, N.; Jiang, X.; Gao, J.; Bai, L.; et al. A Co_3O_4-CDots-C_3N_4 three component electrocatalyst design concept for efficient and tunable CO_2 reduction to syngas. *Nat. Commun.* **2017**, *8*, 1828. [CrossRef] [PubMed]

87. Abbasi, P.; Asadi, M.; Liu, C.; Sharifi-Asl, S.; Sayahpour, B.; Behranginia, A.; Zapol, P.; Shahbazian-Yassar, R.; Curtiss, L.A.; Salehi-Khojin, A. Tailoring the Edge Structure of Molybdenum Disulfide toward Electrocatalytic Reduction of Carbon Dioxide. *ACS Nano* **2017**, *11*, 453–460. [CrossRef] [PubMed]

88. Asadi, M.; Kumar, B.; Behranginia, A.; Rosen, B.A.; Baskin, A.; Repnin, N.; Pisasale, D.; Phillips, P.; Zhu, W.; Haasch, R.; et al. Robust carbon dioxide reduction on molybdenum disulphide edges. *Nat. Commun.* **2014**, *5*, 4470. [CrossRef]

89. Asadi, M.; Kim, K.; Liu, C.; Addepalli, A.V.; Abbasi, P.; Yasaei, P.; Phillips, P.; Behranginia, A.; Cerrato, J.M.; Haasch, R.; et al. Nanostructured transition metal dichalcogenide electrocatalysts for CO_2 reduction in ionic liquid. *Science* **2016**, *353*, 467–470. [CrossRef] [PubMed]

90. Kornienko, N.; Zhao, Y.; Kley, C.S.; Zhu, C.; Kim, D.; Lin, S.; Chang, C.J.; Yaghi, O.M.; Yang, P. Metal-organic frameworks for electrocatalytic reduction of carbon dioxide. *J. Am. Chem. Soc.* **2015**, *137*, 14129–14135. [CrossRef]

91. Zhao, C.; Dai, X.; Yao, T.; Chen, W.; Wang, X.; Wang, J.; Yang, J.; Wei, S.; Wu, Y.; Li, Y. Ionic Exchange of Metal-Organic Frameworks to Access Single Nickel Sites for Efficient Electroreduction of CO_2. *J. Am. Chem. Soc.* **2017**, *139*, 8078–8081. [CrossRef]

92. Zhang, Z.; Xiao, J.; Chen, X.J.; Yu, S.; Yu, L.; Si, R.; Wang, Y.; Wang, S.; Meng, X.; Wang, Y.; et al. Reaction Mechanisms of Well-Defined Metal-N$_4$ Sites in Electrocatalytic CO$_2$ Reduction. *Angew. Chem. Int. Ed.* **2018**, *57*, 16339–16342. [CrossRef] [PubMed]

93. Gao, S.; Jiao, X.; Sun, Z.; Zhang, W.; Sun, Y.; Wang, C.; Hu, Q.; Zu, X.; Yang, F.; Yang, S.; et al. Ultrathin Co$_3$O$_4$ Layers Realizing Optimized CO$_2$ Electroreduction to Formate. *Angew. Chem. Int. Ed.* **2016**, *55*, 698–702. [CrossRef] [PubMed]

94. Gao, S.; Sun, Z.; Liu, W.; Jiao, X.; Zu, X.; Hu, Q.; Sun, Y.; Yao, T.; Zhang, W.; Wei, S.; et al. Atomic layer confined vacancies for atomic-level insights into carbon dioxide electroreduction. *Nature. Commun.* **2017**, *8*, 14503. [CrossRef] [PubMed]

95. Li, F.; Chen, L.; Knowles, G.P.; MacFarlane, D.R.; Zhang, J. Hierarchical Mesoporous SnO$_2$ Nanosheets on Carbon Cloth: A Robust and Flexible Electrocatalyst for CO$_2$ Reduction with High Efficiency and Selectivity. *Angew. Chem. Int. Ed.* **2017**, *56*, 505–509. [CrossRef] [PubMed]

96. Wang, Y.; Chen, Z.; Han, P.; Du, Y.; Gu, Z.; Xu, X.; Zheng, G. Single-Atomic Cu with Multiple Oxygen Vacancies on Ceria for Electrocatalytic CO$_2$ Reduction to CH$_4$. *ACS Catal.* **2018**, *8*, 7113–7119. [CrossRef]

97. Huan, T.N.; Ranjbar, N.; Rousse, G.; Sougrati, M.; Zitolo, A.; Mougel, V.; Jaouen, F.; Fontecave, M. Electrochemical Reduction of CO$_2$ Catalyzed by Fe-N-C Materials: A Structure–Selectivity Study. *ACS Catal.* **2017**, *7*, 1520–1525. [CrossRef]

98. Zhang, C.; Yang, S.; Wu, J.; Liu, M.; Yazdi, S.; Ren, M.; Sha, J.; Zhong, J.; Nie, K.; Jalilov, A.S.; et al. Electrochemical CO$_2$ Reduction with Atomic Iron-Dispersed on Nitrogen-Doped Graphene. *Adv. Energy Mater.* **2018**, *8*, 1703487. [CrossRef]

99. Zhang, H.; Li, J.; Xi, S.; Du, Y.; Hai, X.; Wang, J.; Xu, H.; Wu, G.; Zhang, J.; Lu, J.; et al. A Graphene-Supported Single-Atom FeN$_5$ Catalytic Site for Efficient Electrochemical CO$_2$ Reduction. *Angew. Chem. Int. Ed.* **2019**, *58*, 14871–14876. [CrossRef]

100. Zhang, Z.; Ma, C.; Tu, Y.; Si, R.; Wei, J.; Zhang, S.; Wang, Z.; Li, J.-F.; Wang, Y.; Deng, D. Multiscale carbon foam confining single iron atoms for efficient electrocatalytic CO$_2$ reduction to CO. *Nano Res.* **2019**, *12*, 2313–2317. [CrossRef]

101. Gu, J.; Hsu, C.S.; Bai, L.; Chen, H.M.; Hu, X. Atomically dispersed Fe^{3+} sites catalyze efficient CO$_2$ electroreduction to CO. *Science* **2019**, *364*, 1091–1094. [CrossRef]

102. Yang, F.; Song, P.; Liu, X.; Mei, B.; Xing, W.; Jiang, Z.; Gu, L.; Xu, W. Highly Efficient CO$_2$ Electroreduction on ZnN$_4$-based Single-Atom Catalyst. *Angew. Chem. Int. Ed.* **2018**, *57*, 12303–12307. [CrossRef] [PubMed]

103. Zhao, S.; Chen, G.; Zhou, G.; Yin, L.C.; Veder, J.P.; Johannessen, B.; Saunders, M.; Yang, S.Z.; De Marco, R.; Liu, C.; et al. A Universal Seeding Strategy to Synthesize Single Atom Catalysts on 2D Materials for Electrocatalytic Applications. *Adv. Funct. Mater.* **2019**, *30*, 1906157. [CrossRef]

104. Yang, H.B.; Hung, S.F.; Liu, S.; Yuan, K.; Miao, S.; Zhang, L.; Huang, X.; Wang, H.Y.; Cai, W.; Chen, R.; et al. Atomically dispersed Ni(i) as the active site for electrochemical CO$_2$ reduction. *Nat. Energy* **2018**, *3*, 140–147. [CrossRef]

105. Liu, S.; Yang, H.B.; Hung, S.F.; Ding, J.; Cai, W.; Liu, L.; Gao, J.; Li, X.; Ren, X.; Kuang, Z.; et al. Elucidating the Electrocatalytic CO$_2$ Reduction Reaction over a Model Single-Atom Nickel Catalyst. *Angew. Chem. Int. Ed.* **2020**, *59*, 798–803. [CrossRef]

106. Gong, Y.N.; Jiao, L.; Qian, Y.; Pan, C.Y.; Zheng, L.; Cai, X.; Liu, B.; Yu, S.H.; Jiang, H.L. Regulating the Coordination Environment of MOF-Templated Single-Atom Nickel Electrocatalysts for Boosting CO$_2$ Reduction. *Angew. Chem. Int. Ed.* **2020**, *59*, 2705–2709. [CrossRef]

107. Han, J.; An, P.; Liu, S.; Zhang, X.; Wang, D.; Yuan, Y.; Guo, J.; Qiu, X.; Hou, K.; Shi, L.; et al. Reordering d Orbital Energies of Single-Site Catalysts for CO$_2$ Electroreduction. *Angew. Chem. Int. Ed.* **2019**, *58*, 12711–12716. [CrossRef]

108. Zheng, W.; Yang, J.; Chen, H.; Hou, Y.; Wang, Q.; Gu, M.; He, F.; Xia, Y.; Xia, Z.; Li, Z.; et al. Atomically Defined Undercoordinated Active Sites for Highly Efficient CO$_2$ Electroreduction. *Adv. Func. Mater.* **2019**, *30*, 1907658. [CrossRef]

109. Murata, A.; Hori, Y. Product Selectivity Affected by Cationic Species in Electrochemical Reduction of CO$_2$ and CO at a Cu Electrode. *Bull. Chem. Soc. Jpn.* **1991**, *64*, 123–127. [CrossRef]

110. Qin, B.; Li, Y.; Fu, H.; Wang, H.; Chen, S.; Liu, Z.; Peng, F. Electrochemical Reduction of CO$_2$ into Tunable Syngas Production by Regulating the Crystal Facets of Earth-Abundant Zn Catalyst. *ACS Appl. Mater. Interfaces* **2018**, *10*, 20530–20539. [CrossRef]

111. Jiang, K.; Huang, Y.; Zeng, G.; Toma, F.M.; Goddard, W.A.; Bell, A.T. Effects of Surface Roughness on the Electrochemical Reduction of CO$_2$ over Cu. *ACS Energy Lett.* **2020**, *5*, 1206–1214. [CrossRef]

112. Huang, X.; Tang, S.; Mu, X.; Dai, Y.; Chen, G.; Zhou, Z.; Ruan, F.; Yang, Z.; Zheng, N. Freestanding palladium nanosheets with plasmonic and catalytic properties. *Nat. Nanotechnol.* **2011**, *6*, 28–32. [CrossRef] [PubMed]

113. Mistry, H.; Reske, R.; Zeng, Z.; Zhao, Z.J.; Greeley, J.; Strasser, P.; Cuenya, B.R. Exceptional size-dependent activity enhancement in the electroreduction of CO$_2$ over Au nanoparticles. *J. Am. Chem. Soc.* **2014**, *136*, 16473–16476. [CrossRef]

114. Yang, Q.; Shi, L.; Yu, B.; Xu, J.; Wei, C.; Wang, Y.; Chen, H. Facile synthesis of ultrathin Pt–Pd nanosheets for enhanced formic acid oxidation and oxygen reduction reaction. *J. Mater. Chem. A* **2019**, *7*, 18846–18851. [CrossRef]

115. Gao, F.; Zhang, Y.; Ren, F.; Shiraishi, Y.; Du, Y. Universal Surfactant-Free Strategy for Self-Standing 3D Tremella-Like Pd–M (M = Ag, Pb, and Au) Nanosheets for Superior Alcohols Electrocatalysis. *Adv. Funct. Mater.* **2020**, *30*, 2000255. [CrossRef]

116. Zhang, S.; Fan, Q.; Xia, R.; Meyer, T.J. CO$_2$ Reduction: From Homogeneous to Heterogeneous Electrocatalysis. *Acc. Chem. Res.* **2020**, *53*, 255–264. [CrossRef] [PubMed]

117. Liu, K.; Ma, M.; Wu, L.; Valenti, M.; Cardenas-Morcoso, D.; Hofmann, J.P.; Bisquert, J.; Gimenez, S.; Smith, W.A. Electronic Effects Determine the Selectivity of Planar Au–Cu Bimetallic Thin Films for Electrochemical CO$_2$ Reduction. *ACS Appl. Mater. Interfaces* **2019**, *11*, 16546–16555. [CrossRef] [PubMed]

118. Wu, Z.P.; Lu, X.F.; Zang, S.Q.; Lou, X.W. Non-Noble-Metal-Based Electrocatalysts toward the Oxygen Evolution Reaction. *Adv. Funct. Mater.* **2020**, *30*, 1910274. [CrossRef]

119. Zhu, Y.P.; Guo, C.; Zheng, Y.; Qiao, S.Z. Surface and Interface Engineering of Noble-Metal-Free Electrocatalysts for Efficient Energy Conversion Processes. *Acc. Chem. Res.* **2017**, *50*, 915–923. [CrossRef]

120. Kuhl, K.P.; Cave, E.R.; Abram, D.N.; Jaramillo, T.F. New insights into the electrochemical reduction of carbon dioxide on metallic copper surfaces. *Energy Environ. Sci.* **2012**, *5*, 7050–7059. [CrossRef]

121. Kuang, Y.; Feng, G.; Li, P.; Bi, Y.; Li, Y.; Sun, X. Single-Crystalline Ultrathin Nickel Nanosheets Array from In Situ Topotactic Reduction for Active and Stable Electrocatalysis. *Angew. Chem. Int. Ed.* **2016**, *55*, 693–697. [CrossRef]

122. Zhang, W.; Yang, S.; Jiang, M.; Hu, Y.; Hu, C.; Zhang, X.; Jin, Z. Nanocapillarity and Nanoconfinement Effects of Pipet-like Bismuth@Carbon Nanotubes for Highly Efficient Electrocatalytic CO_2 Reduction. *Nano Lett.* **2021**, *21*, 2650–2657. [CrossRef] [PubMed]

123. Tao, H.; Gao, Y.; Talreja, N.; Guo, F.; Texter, J.; Yan, C.; Sun, Z. Two-dimensional nanosheets for electrocatalysis in energy generation and conversion. *J. Mater. Chem. A* **2017**, *5*, 7257–7284. [CrossRef]

124. Chai, G.L.; Guo, Z.X. Highly effective sites and selectivity of nitrogen-doped graphene/CNT catalysts for CO_2 electrochemical reduction. *Chem. Sci.* **2016**, *7*, 1268–1275. [CrossRef] [PubMed]

125. Duan, X.; Xu, J.; Wei, Z.; Ma, J.; Guo, S.; Wang, S.; Liu, H.; Dou, S. Metal-Free Carbon Materials for CO_2 Electrochemical Reduction. *Adv. Mater.* **2017**, *29*, 201701784. [CrossRef]

126. Liu, Y.; Zhao, J.; Cai, Q. Pyrrolic-nitrogen doped graphene: A metal-free electrocatalyst with high efficiency and selectivity for the reduction of carbon dioxide to formic acid: A computational study. *Phys. Chem. Chem. Phys.* **2016**, *18*, 5491–5498. [CrossRef]

127. Rogers, C.; Perkins, W.S.; Veber, G.; Williams, T.E.; Cloke, R.R.; Fischer, F.R. Synergistic Enhancement of Electrocatalytic CO_2 Reduction with Gold Nanoparticles Embedded in Functional Graphene Nanoribbon Composite Electrodes. *J. Am. Chem. Soc.* **2017**, *139*, 4052–4061. [CrossRef]

128. Zeng, M.; Li, Y. Recent advances in heterogeneous electrocatalysts for the hydrogen evolution reaction. *J. Mater. Chem. A* **2015**, *3*, 14942–14962. [CrossRef]

129. Xie, Y.; Li, X.; Wang, Y.; Li, B.; Yang, L.; Zhao, N.; Liu, M.; Wang, X.; Yu, Y.; Liu, J.M. Reaction mechanisms for reduction of CO_2 to CO on monolayer MoS_2. *Appl. Surf. Sci.* **2020**, *499*, 143964. [CrossRef]

130. Hong, X.; Chan, K.; Tsai, C.; Nørskov, J.K. How Doped MoS_2 Breaks Transition-Metal Scaling Relations for CO_2 Electrochemical Reduction. *ACS Catal.* **2016**, *6*, 4428–4437. [CrossRef]

131. Chan, K.; Tsai, C.; Hansen, H.A.; Nørskov, J.K. Molybdenum Sulfides and Selenides as Possible Electrocatalysts for CO_2 Reduction. *ChemCatChem* **2014**, *6*, 1899–1905. [CrossRef]

132. Shao, P.; Yi, L.; Chen, S.; Zhou, T.; Zhang, J. Metal-organic frameworks for electrochemical reduction of carbon dioxide: The role of metal centers. *J. Energy Chem.* **2020**, *40*, 156–170. [CrossRef]

133. Perfecto-Irigaray, M.; Albo, J.; Beobide, G.; Castillo, O.; Irabien, A.; Pérez-Yáñez, S. Synthesis of heterometallic metal–organic frameworks and their performance as electrocatalyst for CO_2 reduction. *RSC Adv.* **2018**, *8*, 21092–21099. [CrossRef]

134. Majidi, L.; Ahmadiparidari, A.; Shan, N.; Misal, S.N.; Kumar, K.; Huang, Z.; Rastegar, S.; Hemmat, Z.; Zou, X.; Zapol, P.; et al. 2D Copper Tetrahydroxyquinone Conductive Metal-Organic Framework for Selective CO_2 Electrocatalysis at Low Overpotentials. *Adv. Mater.* **2021**, *33*, e2004393. [CrossRef] [PubMed]

135. Chen, Y.; Kanan, M.W. Tin oxide dependence of the CO_2 reduction efficiency on tin electrodes and enhanced activity for tin/tin oxide thin-film catalysts. *J. Am. Chem. Soc.* **2012**, *134*, 1986–1989. [CrossRef] [PubMed]

136. Li, C.W.; Kanan, M.W. CO_2 reduction at low overpotential on Cu electrodes resulting from the reduction of thick Cu_2O films. *J. Am. Chem. Soc.* **2012**, *134*, 7231–7234. [CrossRef]

137. Liu, J.; Guo, C.; Vasileff, A.; Qiao, S. Nanostructured 2D Materials: Prospective Catalysts for Electrochemical CO_2 Reduction. *Small Methods* **2017**, *1*, 1600006. [CrossRef]

138. Yang, X.F.; Wang, A.Q.; Qiao, B.T.; Li, J.; Liu, J.Y.; Zhang, T. Single-Atom Catalysts: A New Frontier in Heterogeneous Catalysis. *Acc. Chem. Res.* **2013**, *46*, 1740–1748. [CrossRef]

139. Wang, A.; Li, J.; Zhang, T. Heterogeneous single-atom catalysis. *Nat. Rev. Chem.* **2018**, *2*, 65–81. [CrossRef]

140. Chorkendorff, I.; Niemantsverdriet, J.W. *Concepts of Modern Catalysis and Kinetics*; Wiley: Weinheim, Germany, 2003. [CrossRef]

141. Jaramillo, T.F.; Jorgensen, K.P.; Bonde, J.; Nielsen, J.H.; Horch, S.; Chorkendorff, I. Identification of Active Edge Sites for Electrochemical H_2 Evolution from MoS_2 Nanocatalysts. *Science* **2007**, *317*, 100–102. [CrossRef]

142. Seh, Z.W.; Kibsgaard, J.; Dickens, C.F.; Chorkendorff, I.; Norskov, J.K.; Jaramillo, T.F. Combining theory and experiment in electrocatalysis: Insights into materials design. *Science* **2017**, *355*, aad4998. [CrossRef]

143. Kyriakou, G.; Boucher, M.W.; Jewell, A.D.; Lewis, E.A.; Lawton, T.J.; Baber, A.E.; Tierney, H.L.; Flytzani-Stephanopoulos, M.; Sykes, E.C. Isolated Metal Atom Geometries as a Strategy for Selective Heterogeneous Hydrogenations. *Science* **2012**, *335*, 1209–1212. [CrossRef] [PubMed]

144. Zhang, N.; Zhou, T.; Chen, M.; Feng, H.; Yuan, R.; Zhong, C.a.; Yan, W.; Tian, Y.; Wu, X.; Chu, W.; et al. High-purity pyrrole-type FeN_4 sites as a superior oxygen reduction electrocatalyst. *Energy Environ. Sci.* **2020**, *13*, 111–118. [CrossRef]

145. Yin, X.P.; Wang, H.J.; Tang, S.F.; Lu, X.L.; Shu, M.; Si, R.; Lu, T.B. Engineering the Coordination Environment of Single-Atom Platinum Anchored on Graphdiyne for Optimizing Electrocatalytic Hydrogen Evolution. *Angew. Chem. Int. Ed.* **2018**, *57*, 9382–9386. [CrossRef] [PubMed]

146. Xiao, M.; Gao, L.; Wang, Y.; Wang, X.; Zhu, J.; Jin, Z.; Liu, C.; Chen, H.; Li, G.; Ge, J.; et al. Engineering Energy Level of Metal Center: Ru Single-Atom Site for Efficient and Durable Oxygen Reduction Catalysis. *J. Am. Chem. Soc.* **2019**, *141*, 19800–19806. [CrossRef]

147. Zhang, H.; Yu, L.; Chen, T.; Zhou, W.; Lou, X.W.D. Surface Modulation of Hierarchical MoS_2 Nanosheets by Ni Single Atoms for Enhanced Electrocatalytic Hydrogen Evolution. *Adv. Funct. Mater.* **2018**, *28*, 1807086. [CrossRef]

148. Li, H.; Wang, L.; Dai, Y.; Pu, Z.; Lao, Z.; Chen, Y.; Wang, M.; Zheng, X.; Zhu, J.; Zhang, W.; et al. Synergetic interaction between neighbouring platinum monomers in CO_2 hydrogenation. *Nat. Nanotechnol.* **2018**, *13*, 411–417. [CrossRef]

149. Ye, S.; Luo, F.; Zhang, Q.; Zhang, P.; Xu, T.; Wang, Q.; He, D.; Guo, L.; Zhang, Y.; He, C.; et al. Highly stable single Pt atomic sites anchored on aniline-stacked graphene for hydrogen evolution reaction. *Energy Environ. Sci.* **2019**, *12*, 1000–1007. [CrossRef]

150. Yuan, J.; Zhang, W.; Li, X.; Yang, J. A high-performance catalyst for methane conversion to methanol: Graphene supported single atom Co. *Chem. Commun.* **2018**, *54*, 2284–2287. [CrossRef]

151. Ramalingam, V.; Varadhan, P.; Fu, H.C.; Kim, H.; Zhang, D.; Chen, S.; Song, L.; Ma, D.; Wang, Y.; Alshareef, H.N.; et al. Heteroatom-Mediated Interactions between Ruthenium Single Atoms and an MXene Support for Efficient Hydrogen Evolution. *Adv. Mater.* **2019**, *31*, e1903841. [CrossRef]

152. Back, S.; Lim, J.; Kim, N.Y.; Kim, Y.H.; Jung, Y. Single-atom catalysts for CO_2 electroreduction with significant activity and selectivity improvements. *Chem. Sci.* **2017**, *8*, 1090–1096. [CrossRef]

153. Jiang, K.; Siahrostami, S.; Zheng, T.T.; Hu, Y.F.; Hwang, S.Y.; Stavitski, E.; Peng, Y.D.; Dynes, J.; Gangisetty, M.; Su, D.; et al. Isolated Ni single atoms in graphene nanosheets for high-performance CO_2 reduction. *Energy Environ. Sci.* **2018**, *11*, 893–903. [CrossRef]

154. Jiao, Y.; Zheng, Y.; Chen, P.; Jaroniec, M.; Qiao, S.Z. Molecular Scaffolding Strategy with Synergistic Active Centers to Facilitate Electrocatalytic CO_2 Reduction to Hydrocarbon/Alcohol. *J. Am. Chem. Soc.* **2017**, *139*, 18093–18100. [CrossRef] [PubMed]

155. Choi, C.; Cai, J.; Lee, C.; Lee, H.M.; Xu, M.; Huang, Y. Intimate atomic Cu-Ag interfaces for high CO_2RR selectivity towards CH_4 at low over potential. *Nano Res.* **2021**, *14*, 3497–3501. [CrossRef]

156. Chen, B.; Li, B.; Tian, Z.; Liu, W.; Liu, W.; Sun, W.; Wang, K.; Chen, L.; Jiang, J. Enhancement of Mass Transfer for Facilitating Industrial-Level CO_2 Electroreduction on Atomic Ni-N_4 Sites. *Adv. Energy Mater.* **2021**, *11*, 2102152. [CrossRef]

157. Yang, Y.; Li, F. Reactor design for electrochemical CO_2 conversion toward large-scale applications. *Curr. Opin. Green Sustain. Chem.* **2021**, *27*, 100419. [CrossRef]

158. Jayashree, R.S.; Mitchell, M.; Natarajan, D.; Markoski, L.J.; Kenis, P.J.A. Microfluidic Hydrogen Fuel Cell with a Liquid Electrolyte. *Langmuir* **2007**, *23*, 6871–6874. [CrossRef]

159. Whipple, D.T.; Finke, E.C.; Kenis, P.J.A. Microfluidic Reactor for the Electrochemical Reduction of Carbon Dioxide: The Effect of pH. *Electrochem. Solid-State Lett.* **2010**, *13*, 9. [CrossRef]

160. Higgins, D.; Hahn, C.; Xiang, C.; Jaramillo, T.F.; Weber, A.Z. Gas-Diffusion Electrodes for Carbon Dioxide Reduction: A New Paradigm. *ACS Energy Lett.* **2018**, *4*, 317–324. [CrossRef]

161. Lees, E.W.; Mowbray, B.A.W.; Parlane, F.G.L.; Berlinguette, C.P. Gas diffusion electrodes and membranes for CO_2 reduction electrolysers. *Nat. Rev. Mater.* **2021**, *7*, 55–64. [CrossRef]

162. Lim, J.; Kang, P.W.; Jeon, S.S.; Lee, H. Electrochemically deposited Sn catalysts with dense tips on a gas diffusion electrode for electrochemical CO_2 reduction. *J. Mater. Chem. A* **2020**, *8*, 9032–9038. [CrossRef]

163. Rabiee, H.; Ge, L.; Zhang, X.; Hu, S.; Li, M.; Yuan, Z. Gas diffusion electrodes (GDEs) for electrochemical reduction of carbon dioxide, carbon monoxide, and dinitrogen to value-added products: A review. *Energy Environ. Sci.* **2021**, *14*, 1959–2008. [CrossRef]

164. Gabardo, C.M.; O'Brien, C.P.; Edwards, J.P.; McCallum, C.; Xu, Y.; Dinh, C.T.; Li, J.; Sargent, E.H.; Sinton, D. Continuous Carbon Dioxide Electroreduction to Concentrated Multi-carbon Products Using a Membrane Electrode Assembly. *Joule* **2019**, *3*, 2777–2791. [CrossRef]

165. Ren, S.X.; Joulié, D.; Salvatore, D.; Torbensen, K.; Wang, M.; Robert, M.; Berlinguette, C.P. Molecular electrocatalysts can mediate fast, selective CO_2 reduction in a flow cell. *Science* **2019**, *365*, 367–369. [CrossRef] [PubMed]